Naval Surface Warfare Center
Carderock Division
West Bethesda, MD 20817-5700

NSWCCD-80-TR–2015/026   **August 2015**

Naval Architecture and Engineering Department
Technical Report

NONLINEAR INTERACTIONS BETWEEN OBLIQUE WIND WAVES

by

Sang Soo Lee
NSWCCD

REPORT DOCUMENTATION PAGE		*Form Approved* *OMB No. 0704-0188*

1. REPORT DATE *(DD-MM-YYYY)*	2. REPORT TYPE	3. DATES COVERED *(From - To)*
27-Aug-2015	Final	1-Jan-2013 – 30-May-2015

4. TITLE AND SUBTITLE

Nonlinear Interactions between Oblique Wind Waves

5a. CONTRACT NUMBER

5b. GRANT NUMBER

5c. PROGRAM ELEMENT NUMBER

6. AUTHOR(S)

Lee, Sang Soo

5d. PROJECT NUMBER

5e. TASK NUMBER

5f. WORK UNIT NUMBER
NWA 100001020887

7. PERFORMING ORGANIZATION NAME(S) AND ADDRESS(ES) AND ADDRESS(ES)

Naval Surface Warfare Center
Carderock Division
9500 Macarthur Boulevard
West Bethesda, MD 20817-5700

8. PERFORMING ORGANIZATION REPORT NUMBER

NSWCCD-80-TR-2015/026

9. SPONSORING / MONITORING AGENCY NAME(S) AND ADDRESS(ES)
Office of the Director of
Research
Naval Surface Warfare Center
Carderock Division
9500 Macarthur Boulevard
West Bethesda, MD 20817-5700

10. SPONSOR/MONITOR'S ACRONYM(S)

11. SPONSOR/MONITOR'S REPORT NUMBER(S)

12. DISTRIBUTION / AVAILABILITY STATEMENT
DISTRIBUTION STATEMENT A. Approved for public release; Distribution is unlimited.

13. SUPPLEMENTARY NOTES

14. ABSTRACT
The nonlinear interaction between two oblique wind waves with the same wave speed is analyzed.
The primary fluctuation, whose steepness is of the order of the cube of the density ratio of air to water, interacts with a secondary fluctuation of smaller steepness.
The case where the secondary-wave frequency is higher than the primary frequency is studied.
The nonlinear interaction generates N difference modes, where N is the smallest integer not less than the ratio of the secondary to primary frequencies. The amplitudes of the nonlinearly generated difference modes can grow faster than exponentially, and they can approach an exponential-of-an-exponential growth stage.

15. SUBJECT TERMS
Wind wave interaction, Wind waves, Nonlinear Interaction, Critical Layer

16. SECURITY CLASSIFICATION OF:			17. LIMITATION OF ABSTRACT	18. NUMBER OF PAGES	19a. NAME OF RESPONSIBLE PERSON T. Smith
a. REPORT UNCLASSIFIED	**b. ABSTRACT** UNCLASSIFIED	**c. THIS PAGE** UNCLASSIFIED	UL	64	**19b. TELEPHONE NUMBER** *(include area code)* 301-227-5117

i

This page intentionally left blank.

CONTENTS

FIGURES

ADMINISTRATIVE INFORMATION

ACKNOWLEDGMENTS

SUMMARY

The nonlinear interaction analysis of wind-driven oblique surface waves by Lee (*J. Fluid. Mech.*, vol. 707, 2012, pp. 150-190) is generalized to include the case where the secondary-wave frequency is higher than the primary frequency. The nonlinear interaction is initiated by two three-dimensional fluctuations in wind, which are induced by oblique surface waves. If both wind waves have the same wave speed in the downwind direction, they share the same critical layer. The primary air fluctuation, whose steepness of the order of the cube of the density ratio of air to water is the largest, then interacts with a secondary fluctuation of smaller steepness in the common critical layer. The critical-layer interaction generates N difference modes, where N is the smallest integer not less than the ratio of the secondary to primary frequencies. The first-difference mode is generated by a nonlinear coupling between the primary and secondary air fluctuations. A subsequent nonlinear interaction between the primary fluctuation and the preceding $(n-1)$th-difference mode generates the succeeding nth-difference mode. However, the critical-layer interaction between the primary and Nth-difference modes completes the difference-mode-generation mechanism by producing a nonlinear effect on the previous $(N-1)$th-difference mode. Only the frequencies of the last two difference modes, the $(N-1)$th and Nth, are lower than the primary frequency. Their amplitudes can grow faster than exponentially, and they soon approach an exponential-of-an-exponential growth stage in the inviscid and finite-viscosity cases.

INTRODUCTION

It is shown by Lee (2012) that the nonlinear critical-layer interactions of three-dimensional fluctuations in air, that are induced by obliquely propagating wind waves, can significantly enhance the growth of one of the corresponding surface waves. The critical layer is a thin horizontal region surrounding the critical level at which the mean wind velocity equals the wave speed in the downwind direction. The $2+1$ mode interaction in Lee (2012) is composed of two wind-driven oblique surface waves, referred to as the primary and secondary waves, and one difference mode. The primary wave is the largest oblique wave in the initial stage. The initial steepness of a secondary wave is smaller than the primary one. The $2+1$ mode interaction can occur when both surface waves have the same wave speed in the downwind direction and the frequency of a secondary wave is lower than the primary frequency. The primary and secondary waves grow exponentially in the initial stage of wind wave development wherein the wave steepness is small (Miles, 1957). Once the steepness of the primary wave becomes sufficiently large, the $2+1$ mode interaction can enhance the growth of the secondary and difference modes. A single difference mode is generated by the critical-layer interaction of the primary and secondary waves when the frequency of the latter is lower than the former.

In this paper, the case where the frequency of a secondary wave is higher than the primary frequency will be investigated. More than one difference mode will be generated by critical-layer interactions. Among them, the difference modes whose frequencies are lower than the primary frequency can be greatly amplified due to nonlinear effects. This mechanism may be responsible for generating lower-frequency air fluctuations over surface waves.

A three-dimensional air fluctuation can be induced by a surface wave propagating obliquely to the downwind direction. The corresponding air fluctuation has the same wave characteristics, i.e. frequency and wavenumbers, as the surface wave. The fluctuation in wind is governed by Rayleigh's stability equation and the wave motion in water is irrotational. They are coupled through the interface conditions. As shown by the linear theory of Miles (1957), the wave-induced air fluctuation can be

unstable. The air fluctuation and, consequently, the corresponding surface wave can grow due to the energy transfer from wind to air fluctuation.

The linear growth rate of a surface wave by this resonant wind-wave interaction is proportional to the density ratio of air to water whose typical value is $O(10^{-3})$, as shown by Miles (1957). Since it is small, the leading-order Rayleigh's stability equation becomes singular at the critical level where nonlinear effects first come into play (Davis 1969; Benney & Bergeron 1969; Drazin & Reid 2004). If a secondary wave has the same wave speed in downwind direction as the primary wave, both primary and secondary fluctuations in air share the same critical layer. A nonlinear interaction between them can occur when the steepness of a primary wind wave becomes of the order of the cube of the density ratio of air to water as found in Lee (2012). The secondary wave can be any oblique wind wave of the same wave speed in downstream direction whose steepness is smaller than the primary one. By using a matched asymptotic analysis as in Reutov (1980), Goldstein & Choi (1989), Goldstein & Lee (1992), Wu (1992), Wu & Stewart (1996), Lee & Wundrow (2011), and others, Lee (2012) showed that the $2 + 1$ mode critical-layer interaction induced by two oblique wind waves could enhance the growth of a secondary wind wave.

In a $2 + 1$ mode interaction, the primary-wave frequency is higher than the secondary frequency. The critical-layer interaction between the primary and secondary fluctuations generates a difference mode whose frequency and wavenumbers are equal to the differences between the primary and secondary values. Its amplitude becomes as large as the secondary amplitude in air, but smaller than the latter in water since the difference mode does not satisfy the free-surface-wave dispersion relation. In addition, the nonlinear coupling between the primary and difference modes produces a parametric-growth effect on the secondary wind wave. The primary wave remains linear throughout the whole stage. However, the growth rate of a secondary wave becomes much larger than its linear growth rate, and both secondary and difference mode amplitudes can grow like the exponential-of-an-exponential. The dynamics of a 2+1 mode interaction are similar to those of the phase-locked interaction of Wu & Stewart (1996).

In the present study, the critical-layer analysis of Lee (2012) is extended so that the secondary frequency can be higher than the primary frequency. The nonlinear interaction is still induced by two wind-driven oblique surface waves. As in Lee (2012), the magnitude of a primary oblique wave is of the order of the cube of the density ratio of air to water, and that of a secondary oblique wave is smaller than the primary one. The critical-layer interaction generates N difference modes, where N is the smallest integer not less than the ratio of the secondary to primary frequencies. This interaction is composed of two wind-driven surface waves and N nonlinearly generated difference modes and might be termed the '$2 + N$ mode critical-layer interaction.' The $2 + 1$ mode interaction in Lee (2012) is the simplest case when $N = 1$ that involves only three modes. The analysis of a generalized $2 + N$ mode interaction shows that both primary and secondary waves remain linear if $N \geq 2$. The first $N - 2$ difference modes also grow exponentially although they are nonlinearly generated. The amplitudes of the last two difference modes, the $(N - 1)$th and Nth, are determined by coupled integral equations. They can grow faster than exponentially. Numerical results will show that they can grow like the exponential-of-an-exponential, similar to the secondary and difference modes in the $N = 1$ case. The exponential-of-an-exponential growth only occurs to the modes whose frequencies are lower than the primary-wave frequency. They are the $(N - 1)$th and Nth difference modes if $N \geq 2$, or the secondary and difference modes when $N = 1$.

The linear and nonlinear effects appear at the same order in the amplitude equations in these analyses. Thus, the analysis covers both linear and nonlinear stages and it describes how the nonlinear critical-layer interaction gradually evolves from the interaction between linear wind waves of small

steepnesses. In the initial stage where the primary-wave steepness is smaller than O(the density ratio cubed), the nonlinear amplitude equations reduce to the linear equations.

The $2 + N$ mode analysis ($N \geq 1$) shows that a nonlinear interaction can occur even when the steepness of the largest primary oblique wave is relatively small, i.e. O(the density ratio cubed) or $O(10^{-9})$. The nonlinear critical-layer interaction could be an efficient mechanism by which the difference modes and secondary wave (when $N = 1$) quickly grow as large as the primary wave. Nonlinear interactions in subsequent stages will be more involved since all modes are of the same order of magnitude. Lee & Wundrow (2011) show that the modal growth can be governed by a cubic self-interaction mechanism (Goldstein & Choi 1989) if the wave steepness becomes O(the density ratio raised to the power 5/2).

The findings of enhanced growth of oblique waves are consistent with previous instability wave analyses. It has been shown by various studies that nonlinear critical-layer interactions of oblique instability waves in single-fluid flows produce much larger growth effect than the linear interaction does. Meanwhile, the critical-layer analysis of a plane surface wave, that propagates along the downwind direction, by Reutov (1980) shows that the nonlinear effect reduces the growth rate, even when the wave steepness is as small as O(the density ratio squared) (also in Alexakis, Young & Rosner 2004).

It is also found in Lee (2012) that a linear plane wave remains passive although it is larger than the primary oblique wind wave of O(the density ratio cubed) in the $2 + 1$ mode interaction stage. The direct critical-layer coupling between the plane and oblique wind waves does not produce a nonlinear effect outside the critical layer since the frequency of the plane wave is always lower than the frequencies of oblique waves of an equal wave speed in downwind direction. However, the plane wind wave can interact with the nonlinearly generated difference modes whose frequencies are lower than the plane-wave frequency through the phase-locked interaction of Wu & Stewart (1996).

The analysis in this paper is similar to that in Lee (2012). In fact, the previous $2 + 1$ mode analysis can be included in the current $2 + N$ mode analysis as a special case where $N = 1$. For simplicity, however, the presentation in the main body will be given for $N \geq 2$. Parts of the analysis and discussion that were presented in Lee (2012) will not be repeated. We have tried to keep the same notations as in Lee (2012) for easy cross-referencing. However, a change occurred for the normalization of variables in the final amplitude equations. In Lee (2012), the variables in the final results are normalized by using the properties of the primary and secondary waves of each set of interactions, which simplified the amplitude equations. In this paper, the properties of a wind wave with a 30° propagation angle are used in all cases so that the numerical results of different sets of interactions can be directly compared.

FORMULATION

A right-handed Cartesian coordinate system (x, y, z) with unit vectors $(\boldsymbol{i}, \boldsymbol{j}, \boldsymbol{k})$ is attached to the mean water surface with x in the downwind or streamwise direction of the wind, y in the spanwise lateral direction, and z in the vertical direction, as shown in Figure 1. We suppose that the mean wind is two-dimensional and there is no mean motion in the water. All lengths, velocities, pressures and time in both fluids are non-dimensionalized by Δ_a, U_a, $\rho_a U_a^2$ and Δ_a/U_a, respectively, where Δ_a and U_a will be chosen as in equation (8). The Reynolds numbers are assumed to be large, so viscous effects only enter through the critical layer. The effect of surface tension is not included. The air and water are assumed incompressible and their density ratio is defined as

$$\rho_a/\rho_w = \sigma, \tag{1}$$

where the subscripts a and w denote the quantities of air and water, respectively, and $\sigma \ll 1$ characterizes the small density ratio of air to water.

Perturbation to the air-water interface about the mean water surface, $z = 0$, is described by

$$z = \epsilon \tilde{h}(x, y, t), \tag{2}$$

where ϵ is a measure of a wave steepness and $\tilde{h}$ is a scaled wave elevation. The scaling relation between ϵ and σ will be determined by the dynamics in the critical layer. The critical layer surrounds the critical level where the mean wind velocity equals the wave speed in the streamwise direction.

The total velocity $\boldsymbol{u} = \boldsymbol{i}u + \boldsymbol{j}v + \boldsymbol{k}w$ and pressure p in air are composed of a steady wind and mean pressure plus wave-induced perturbations $\tilde{\boldsymbol{u}} = \boldsymbol{i}\tilde{u} + \boldsymbol{j}\tilde{v} + \boldsymbol{k}\tilde{w}$ and $\tilde{p}$,

$$\boldsymbol{u} = \boldsymbol{i}U(z) + \epsilon\tilde{\boldsymbol{u}}(\boldsymbol{x}, t), \qquad p = P_0 - Gz + \epsilon\tilde{p}(\boldsymbol{x}, t), \tag{3}$$

where $U(z)$ is the steady wind and P_0 denotes the mean pressure. The gravity parameter is defined as

$$G \equiv \mathrm{g}\Delta_a/U_a^2, \tag{4}$$

where g denotes the acceleration due to gravity. It is assumed that the mean velocity at the air-water interface vanishes, i.e.

$$U(0) = 0. \tag{5}$$

The fluid motion in water is irrotational. The velocity and pressure where $z < \epsilon\tilde{h}$ are expressed as

$$\boldsymbol{u} = \epsilon\boldsymbol{\nabla}\tilde{\phi}(\boldsymbol{x}, t), \qquad p = P_0 - (1/\sigma)Gz + (\epsilon/\sigma)\tilde{p}_w. \tag{6}$$

Motions of air and water are coupled at the interface defined by (2). The kinematic interface condition requires that the interface be a material surface for both fluid flows. The pressure at the interface must be continuous according to the dynamic interface condition.

A logarithmic profile is used for the mean wind as in Miles (1957, 1993), Morland & Saffman (1993), Janssen (2004), Lee (2012), and others,

$$U = 2.5\ln(9.025z + 1). \tag{7}$$

The velocity and length in the above turbulent wind profile are non-dimensionalized by

$$U_a = u_*, \qquad \Delta_a = 9.025z_o, \tag{8}$$
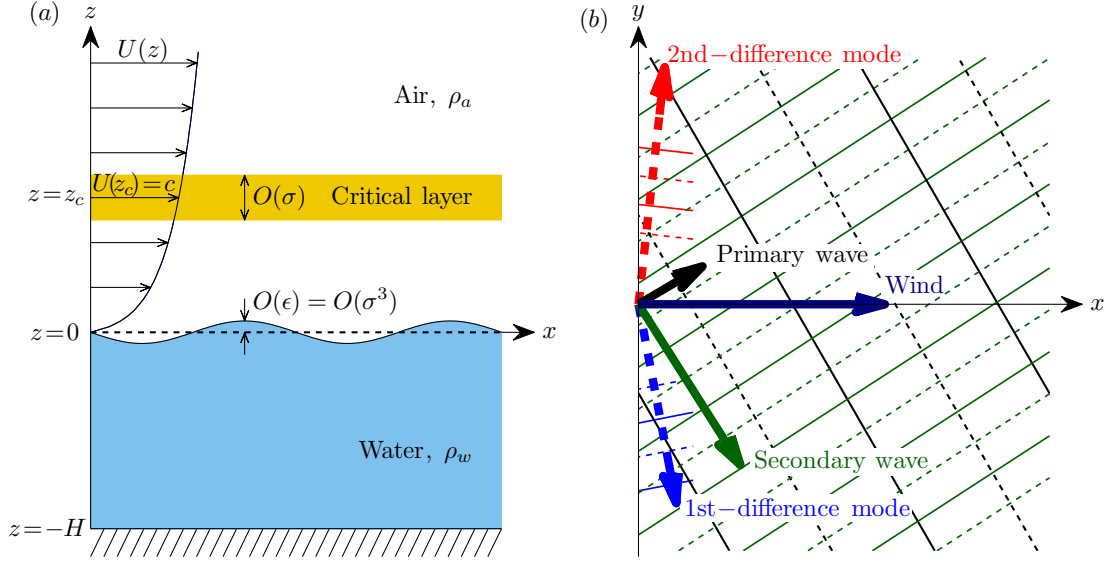
Figure 1. (a) Schematic diagram of a flow field. (b) Wave field of a $2+2$ mode interaction with wave propagation angles of $\theta_p = 30°$, $\theta_s = -57°$, $\theta_{d1} \approx -79°$ and $\theta_{d2} \approx 83.5°$, for the primary, secondary, 1st-difference and 2nd-difference modes. The wave crests are plotted as solid lines and troughs are as dashed lines.

where u_* denotes the friction velocity and z_o is the roughness length. It is worth mentioning that the present analysis is developed for general wind profiles. The specific form (7) will only be used when the final equations are numerically evaluated.

NONLINEAR CRITICAL-LAYER INTERACTIONS

A nonlinear interaction mechanism that is termed the '$2 + N$ mode critical-layer interaction' will be described in this section before we show detailed analyses. A $2 + N$ mode interaction is composed of two wind-driven oblique surface waves and N nonlinearly generated difference modes. Diagrams of interactions for various values of N are shown in Figures 2–4. A representative wave field by a $2 + 2$ mode interaction is illustrated in Figure 1(b).

For each wind-driven surface wave, there exists a corresponding air fluctuation of the same frequency and wavenumbers. The air fluctuation that is not associated with a wind wave can also produce a perturbation in water. The motion of air fluctuation, that is governed by Rayleigh's equation, is coupled with the irrotational motion in water through the interface conditions on the water surface (Miles 1957). During the nonlinear stage of this analysis, only the dynamics of air fluctuations inside the thin critical layer are governed by nonlinear equations. Outside the critical layer, the nonlinear terms in the momentum equations become insignificant and the fluid motions are described by linear equations.

The dispersion relations of wind waves are affected by the dynamics of fluctuations in the air. This effect becomes of a higher order in the present small density ratio case. The leading-order dispersion relations of wind waves equal the dispersion relations of free-surface waves. However, the wavenumbers and frequencies of nonlinearly generated modes are determined by nonlinear interactions. If they do not satisfy the free-surface-wave dispersion relations (at the leading order), the corresponding perturbations in water will disappear when the nonlinearly generated air fluctuations or nonlinear critical-layer effects vanish.

It is assumed that a primary wind wave, denoted by the letter P in Figures 2–4, is the largest oblique surface wave in an initial linear wave field. It is periodic in the form

$$\exp[\mathrm{i}\alpha_p(x - ct) + \mathrm{i}\beta_p y], \tag{9}$$

where $\mathrm{i} \equiv \sqrt{-1}$, c is the wave speed in the streamwise direction, and α_p and β_p are the streamwise and spanwise wavenumbers, respectively. A secondary wind wave of the same c, denoted by S or $\bar{S}$ in the figures, is proportional to

$$\exp[\mathrm{i}\alpha_s(x - ct) + \mathrm{i}\beta_s y]. \tag{10}$$

The streamwise wavenumber α_s, or frequency $\omega_s(= \alpha_s c)$, of a secondary wave can be arbitrarily chosen.

Both primary and secondary waves satisfy the free-surface-wave dispersion relation at the leading order. The relation given in Lee (2012) is written as

$$\beta_\imath^2 = \left[c^4\alpha_\imath^2/\{G^2\tanh^2(\gamma_\imath H)\} - 1\right]\alpha_\imath^2, \quad \text{or} \quad c^2 = (G\gamma_\imath/\alpha_\imath^2)\tanh(\gamma_\imath H), \tag{11}$$

for $\imath = \{p, s\}$, where

$$\gamma_\imath \equiv \sqrt{\alpha_\imath^2 + \beta_\imath^2}, \tag{12}$$

H is the depth of water, and G is defined by (4). The quantities of the primary and secondary waves are denoted with the subscripts p and s, respectively. The wave propagation angle with respect to the streamwise direction, $\theta_\imath$, becomes

$$\theta_\imath = \arctan(\beta_\imath/\alpha_\imath), \quad \cos\theta_\imath = \alpha_\imath/\gamma_\imath, \quad \sin\theta_\imath = \beta_\imath/\gamma_\imath, \quad \text{for} \quad \imath = \{p, s\}, \tag{13}$$

where $-\pi/2 \le \theta_\imath \le \pi/2$.

A contour line of constant c from (11) is plotted in Figures 2(a, b)–4(a, b) when

$$c = 10, \quad G = 0.05, \quad H = 10^{35}. \tag{14}$$

For all wind waves on this curve, $c = 10$. Note that $d|\beta_\imath|/d\alpha_\imath > 0$ and $d|\theta_\imath|/d\alpha_\imath > 0$ for $\imath = \{p, s\}$, which can be proved from (11)–(13). All numerical results are evaluated using the parameter values listed in (14). The large value of H produces the results in deep water. The contour line is replotted in Figures 2(c–h)–4(c–h) as a dotted curve. The primary-wave propagation angles, θ_p, are 30°, 50° and 70° in Figures 2, 3 and 4, respectively.

Because the secondary wave has the same c as the primary wave, they share the same critical level. As found in Lee (2012), a nonlinear interaction between these initially linear wind waves first occurs in their common critical layer when the primary-wave steepness, ϵ, becomes $O(\sigma^3)$. The steepness of the secondary wave is assumed to be smaller than the primary one.

All harmonics, sum and difference modes of the primary and secondary waves, or of any two interacting modes, are generated by quadratic interactions inside the critical layer (details will be given later in (76)). Among them, only the difference mode, whose frequency and wavenumbers are equal to the differences between those of two interacting modes, becomes finite at the outer edges of the critical layer (as will be shown in (83)). The other nonlinearly generated modes become negligibly small outside the critical layer. The difference-mode amplitude becomes as large as the secondary-wave amplitude in the air. If the difference mode is an unsteady oblique mode, it can interact with the primary wave. As will be described in the following subsections, the number of difference modes, N, generated by a $2 + N$ mode interaction becomes

$$N = \mathrm{ceiling}(\omega_s/\omega_p) = \mathrm{ceiling}(\alpha_s/\alpha_p), \tag{15}$$

where the ceiling function denotes the smallest integer not less than its argument, and $\omega_p = \alpha_p c$. In other words, the critical-layer interaction generates N difference modes, if

$$(N-1)\,\omega_p < \omega_s < N\omega_p, \quad (N-1)\alpha_p < \alpha_s < N\alpha_p, \tag{16}$$

where $N \geq 1$. All nonlinearly generated difference modes have the same c as the primary and secondary waves. Since a plane wind wave does not directly interact with oblique wind waves in the nonlinear stage of this analysis, α_p and α_s must be greater than the wavenumber of a corresponding plane wave, $\alpha_{2D} = (G/c^2)\tanh(\alpha_{2D}H)$.

$2 + 1$ mode critical-layer interaction: enhanced growth of a secondary wave

The $2 + 1$ mode interaction between two wind waves and a single nonlinear mode can occur when

$$N = 1 \quad \mathrm{or} \quad \alpha_s < \alpha_p, \tag{17}$$

as studied in Lee (2012). The nonlinear interaction between the primary and secondary modes, denoted by P and S in Figures 2(c, d)–4(c, d), generates a difference mode, denoted by D. Its wavenumbers are $(\alpha_p - \alpha_s, \beta_p - \beta_s)$ and velocity fluctuation is periodic in the form

$$\exp[\mathrm{i}(\alpha_p - \alpha_s)(x - ct) + \mathrm{i}(\beta_p - \beta_s)y], \tag{18}$$

and the propagation angle becomes

$$\theta_d = \arctan[(\beta_p - \beta_s)/(\alpha_p - \alpha_s)]. \tag{19}$$
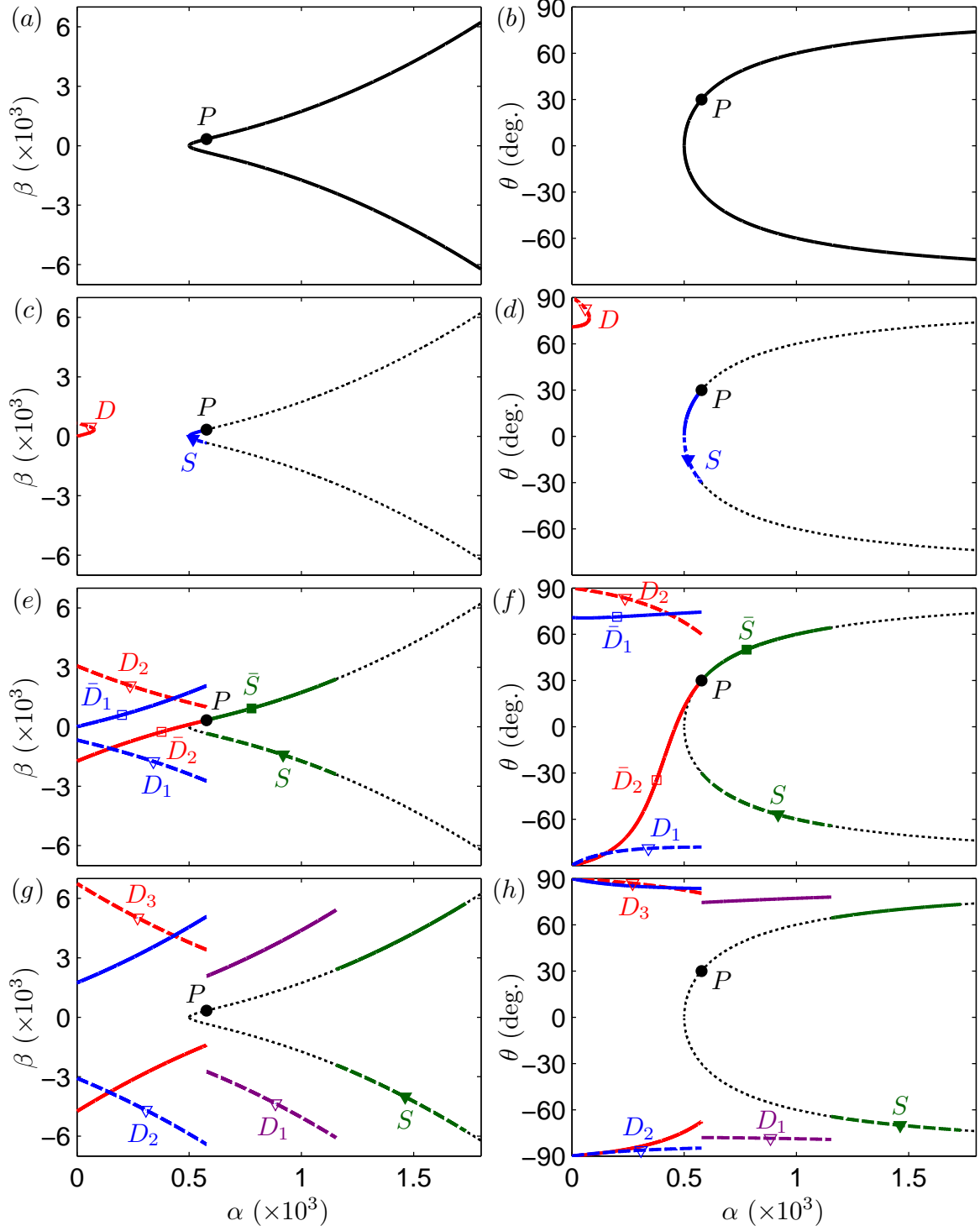
Figure 2. Diagrams of $2 + N$ mode critical-layer interactions when $\theta_p = 30°$. (a, b) The contour line of the free-surface-wave dispersion relation of constant $c = 10$ in the (α, β) and (α, θ) coordinates, with $G = 0.05$ and $H = 10^{35}$. Diagrams of (c, d) $2 + 1$; (e, f) $2 + 2$; (g, h) $2 + 3$ mode critical-layer interactions. The α represents the streamwise wavenumbers, α_p, α_s and $|\alpha_s - n\alpha_p|$, for the primary, secondary and nth-difference modes, and β and θ are the spanwise wavenumber and wave propagation angle of the corresponding mode.

8
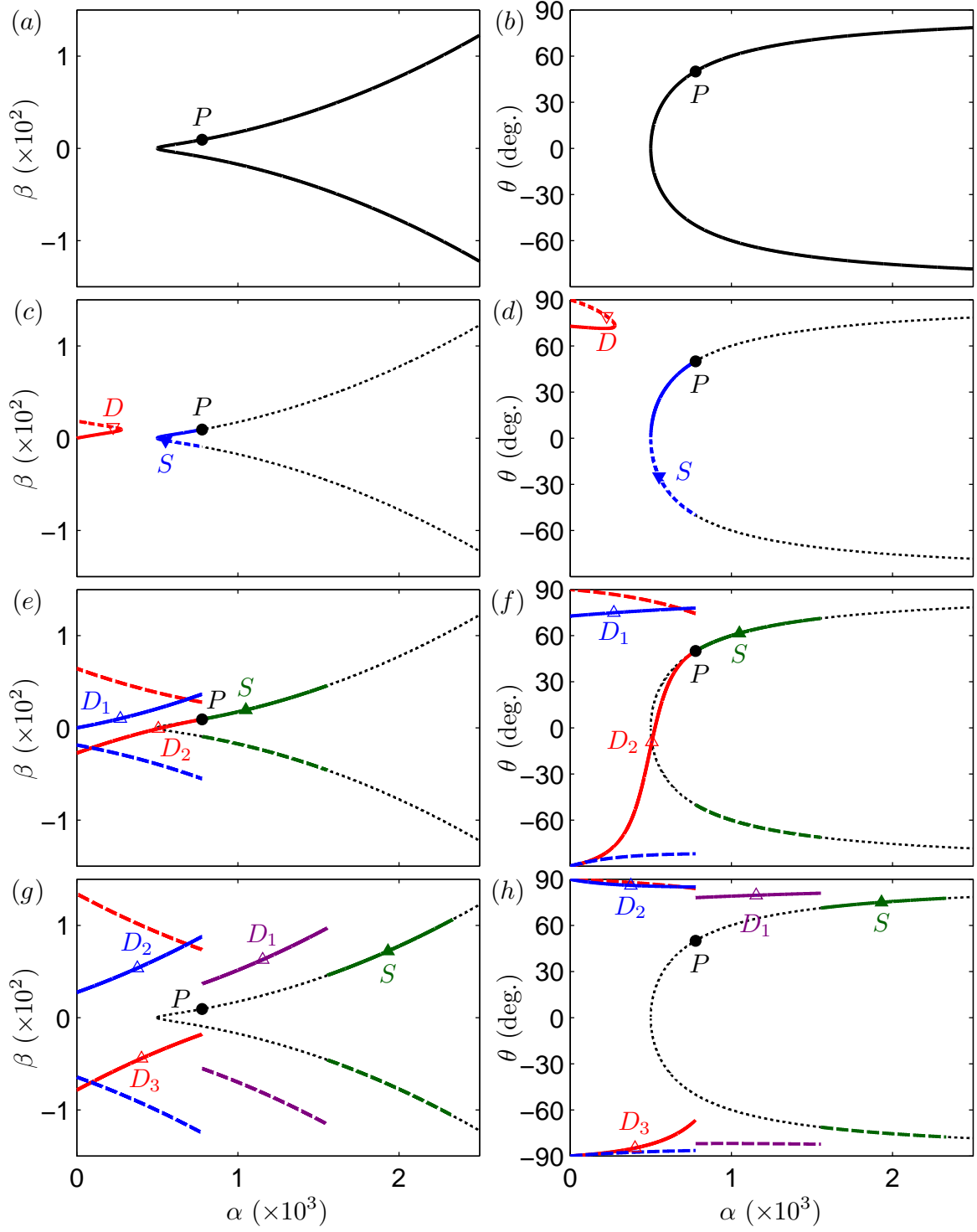
Figure 3. Diagrams of $2 + N$ mode critical-layer interactions when $\theta_p = 50°$. (a, b) The same $c = 10$ contour line as in Figures 2(a, b). Diagrams of (c, d) $2 + 1$; (e, f) $2 + 2$; (g, h) $2 + 3$ mode critical-layer interactions.
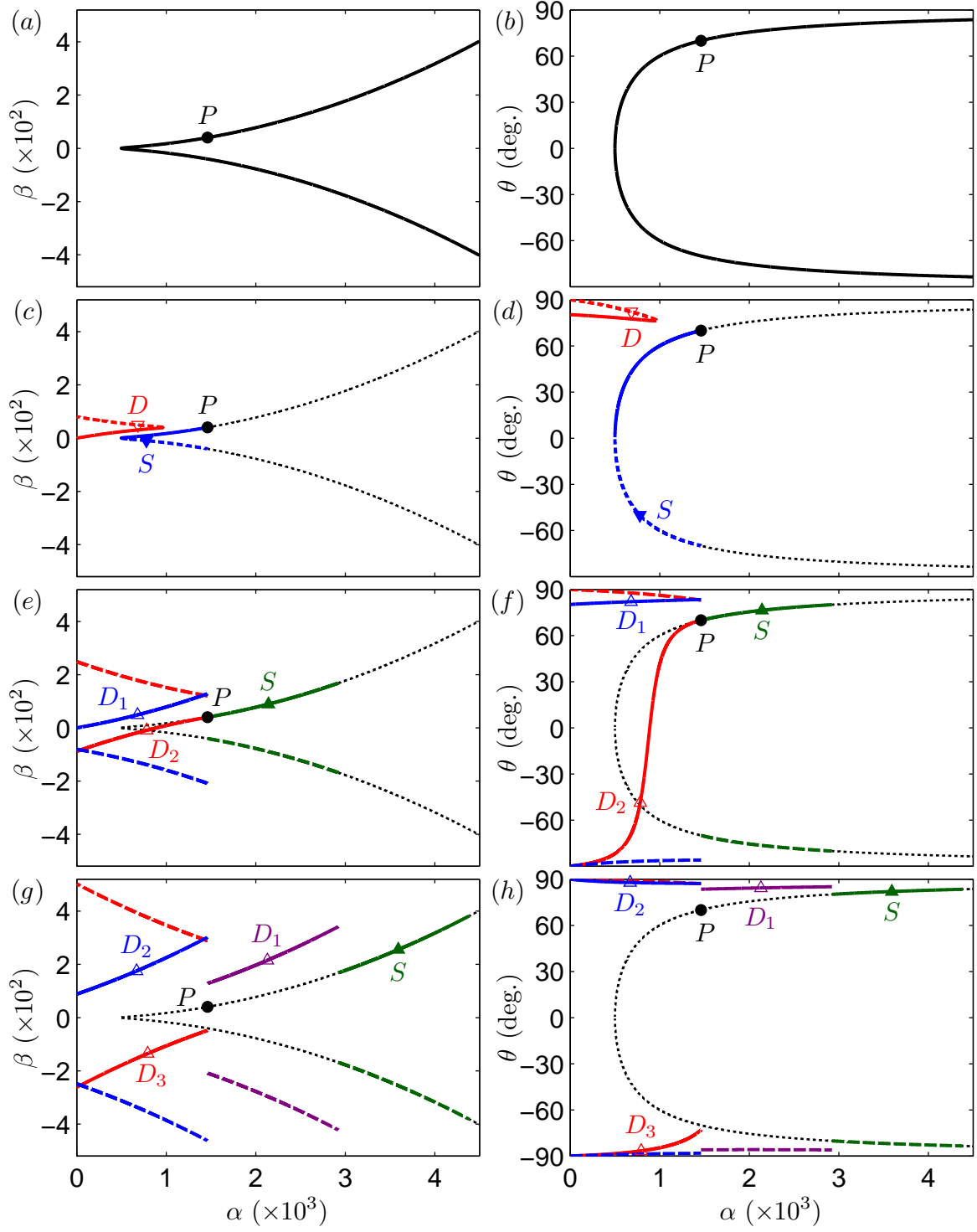
Figure 4. Diagrams of $2 + N$ mode critical-layer interactions when $\theta_p = 70°$. (a, b) The same $c = 10$ contour line as in Figures 2(a, b). Diagrams of (c, d) $2 + 1$; (e, f) $2 + 2$; (g, h) $2 + 3$ mode critical-layer interactions.
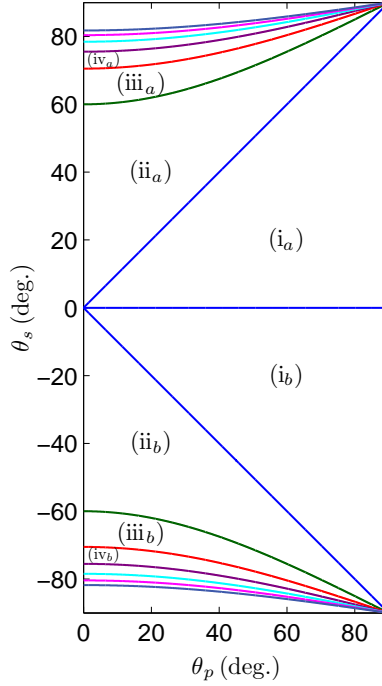
Figure 5. Conditions on (θ_p, θ_s) for various $2+N$ mode interactions. In regions $(i_{a,b})$, $N = 1$; $(ii_{a,b})$, $N = 2$; $(iii_{a,b})$, $N = 3$; $(iv_{a,b})$, $N = 4$. The regions where $N = 5$, 6 and 7 are plotted without labels. Border lines for $N \geq 8$ are not plotted since regions become too narrow. Parameter values in (14) were used.

Meanwhile, the critical-layer interaction between the primary and difference modes produces a nonlinear effect on the secondary wind wave. The amplitudes of the secondary and difference modes are governed by an integro-differential and integral equations, respectively, and they can grow faster than exponentially. The primary wave remains linear. The frequencies of the secondary and difference modes, ω_s and ω_d $(= \omega_p - \omega_s)$, are lower than the primary frequency ω_p.

The primary wave P in Figures 2(c, d)–4(c, d) can also interact with any secondary wave on blue curves to generate a difference mode on red curves. Any combination of (θ_p, θ_s) in both triangular regions $(i_{a,b})$ in Figure 5 produces a $2+1$ mode interaction. The contour lines of constant θ_d are shown in regions $(i_{a,b})$ in Figure 6(a). For simplicity, we only show the results when $\theta_p > 0$ in the figures.

$2+2$ mode critical-layer interaction: generation of two difference modes

More than one difference mode is generated if the secondary frequency is larger than the primary frequency. If

$$N = 2 \quad \text{or} \quad \alpha_p < \alpha_s < 2\alpha_p, \tag{20}$$

the critical-layer interaction between the primary and secondary modes, P and S in Figures 2(e, f)–4(e, f), generates a first-difference mode D_1. Its wavenumbers are $(\alpha_s - \alpha_p, \beta_s - \beta_p)$ and it is periodic in the form $\exp[i(\alpha_s - \alpha_p)(x - ct) + i(\beta_s - \beta_p)y]$, and the propagation angle θ_{d1} equals θ_d given by (19). Then, the subsequent quadratic coupling between P and D_1 produces a second-difference mode D_2.

11
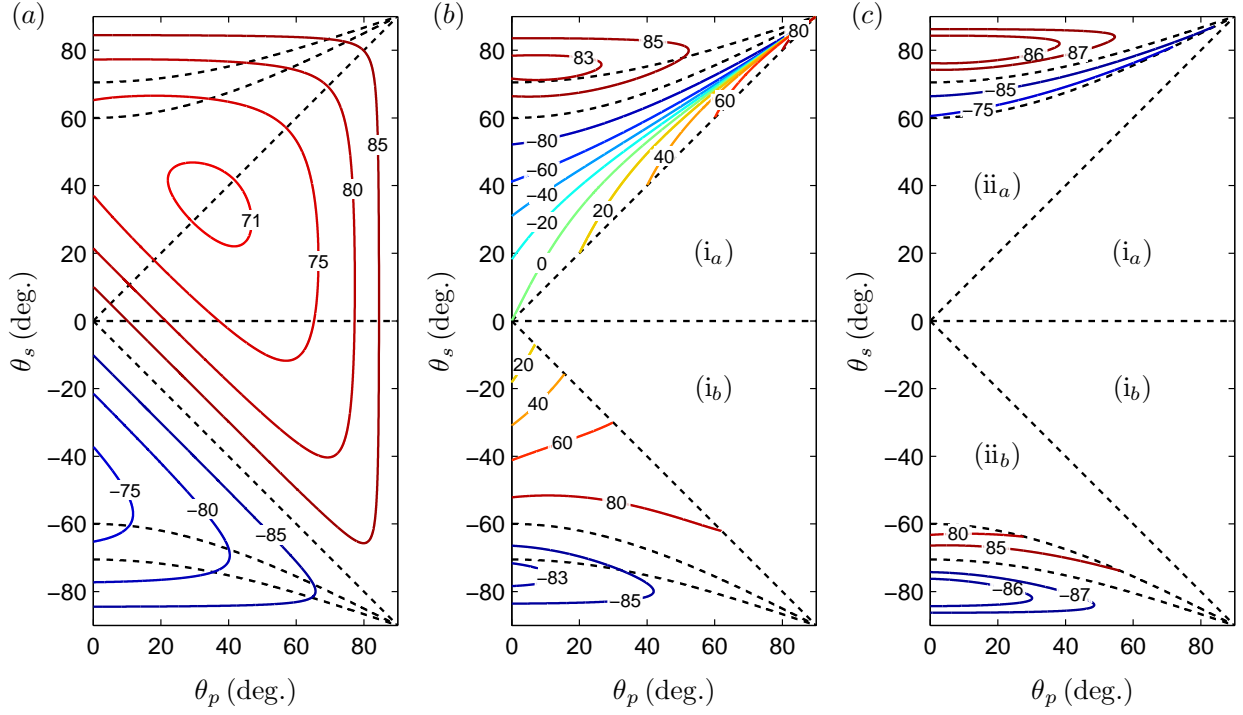
Figure 6. Contour lines of constant wave propagation angles of difference modes in the (θ_p, θ_s) plane. (a) θ_{d1}; (b) θ_{d2}; (c) θ_{d3}. Border lines of regions $(i_{a,b})$, $(ii_{a,b})$ and $(iii_{a,b})$ shown in Figure 5 are replotted as black dotted curves. Regions $(iii_{a,b})$ are located above and below regions $(ii_{a,b})$ as in Figure 5. Units of contour-line labels are degrees.

With wavenumbers of $(2\alpha_p - \alpha_s, 2\beta_p - \beta_s)$, it is proportional to

$$\exp[\mathrm{i}(2\alpha_p - \alpha_s)(x - ct) + \mathrm{i}(2\beta_p - \beta_s)y].\tag{21}$$

The propagation angle of D_2 becomes

$$\theta_{d2} = \arctan[(2\beta_p - \beta_s)/(2\alpha_p - \alpha_s)].\tag{22}$$

Since the wavenumber differences between P and D_2 are equal to the wavenumbers of D_1, the next nonlinear interaction of the primary and 2nd-difference modes produces a nonlinear effect on the 1st-difference mode. Both primary and secondary waves remain linear. The amplitudes of the first and second difference modes are governed by integral equations, and they can grow faster than exponentially as will be shown later. The frequencies of both difference modes, ω_{d1} $(= \omega_s - \omega_p)$ and ω_{d2} $(= 2\omega_p - \omega_s)$, are lower than the primary-wave frequency ω_p. The wave field by the $2 + 2$ mode interaction of four modes P, S, D_1 and D_2 in Figures 2(e, f) is illustrated in Figure 1(b).

The $2 + 2$ mode interaction by P and $\bar{S}$ in Figures 2(e, f) generates the difference modes $\bar{D}_1$ and $\bar{D}_2$. The interaction of P and any secondary wave located on green solid or dashed curve in Figures 2(e, f)–4(e, f) generates the 1st and 2nd difference modes on the corresponding blue and red curves. The $2 + 2$ mode interaction occurs in regions $(\mathrm{ii}_{a,b})$ in Figure 5. The contour lines of constant θ_{d1} and θ_{d2} are plotted in Figures 6(a, b).

It is interesting to note that θ_{d2} can become zero in region (ii_a) in Figure 6(b). Figures 2(f)–4(f) also show that a $2 + 2$ mode interaction can generate a plane second-difference mode. The condition for this case will be given later.

The 2nd-difference mode can be a wind wave as shown in Figures 3(e, f) and 4(e, f) for the $\theta_p = 50°$ and $70°$ cases. The $2 + 2$ mode interaction by P and S generates the difference modes D_1 and D_2. Since the 2nd-difference mode D_2 is located on the black dotted curve, it satisfies the free-surface-wave dispersion relation at the leading order. This is an interesting case where a $3 + 1$ mode interaction between three wind waves and one difference mode occurs.

$2 + N$ mode critical-layer interaction: generation of N difference modes

Previous $2 + 2$ mode interaction mechanism can be extended for an arbitrary value of $N \geq 2$. Two wind waves and N difference modes are involved in a $2 + N$ mode interaction. Diagrams of interactions when $N = 3$ are shown in Figures 2(g, h)–4(g, h).

When

$$N \geq 2 \quad \text{and} \quad (N-1)\alpha_p < \alpha_s < N\alpha_p,\tag{23}$$

the 1st-difference mode D_1 in the Figures is generated by the nonlinear interaction of the primary and secondary modes, P and S, as in the $2 + 2$ mode interaction. The subsequent quadratic interaction between the primary wave P and the preceding $(n - 1)$th-difference mode D_{n-1} keeps generating the succeeding nth-difference mode D_n until the last Nth-difference mode D_N is generated. For $1 \leq n \leq N - 1$, the wavenumbers of the nth-difference mode become $(\alpha_s - n\alpha_p, \beta_s - n\beta_p)$ and the velocity fluctuation is periodic in the form

$$\exp[\mathrm{i}(\alpha_s - n\alpha_p)(x - ct) + \mathrm{i}(\beta_s - n\beta_p)y] \quad \text{if} \quad 1 \leq n \leq N - 1,\tag{24}$$

Its wave propagation angle becomes

$$\theta_{dn} = \arctan[(\beta_s - n\beta_p)/(\alpha_s - n\alpha_p)] \quad \text{if} \quad 1 \leq n \leq N - 1.\tag{25}$$

13

The Nth-difference mode, with wavenumbers of $(N\alpha_p - \alpha_s, N\beta_p - \beta_s)$, is periodic in the form

$$\exp[\mathrm{i}(N\alpha_p - \alpha_s)(x - ct) + \mathrm{i}(N\beta_p - \beta_s)y] \quad \text{if} \quad n = N, \tag{26}$$

and its wave propagation angle becomes

$$\theta_{dN} = \arctan[(N\beta_p - \beta_s)/(N\alpha_p - \alpha_s)]. \tag{27}$$

As expected from the $2 + 1$ and $2 + 2$ mode interactions, the difference-mode-generation mechanism is completed by the interaction of the primary and Nth-difference modes since their wavenumber differences are equal to the wavenumbers of the $(N - 1)$th-difference mode. Thus, the coupling between P and D_N produces a nonlinear effect on D_{N-1}. The linear primary and secondary waves grow exponentially. Although it is nonlinearly generated, the nth-difference mode also grows exponentially for $1 \le n \le N-2$. Their frequencies, ω_{dn} $(= \omega_{d(n-1)} - \omega_p)$, are higher than the primary frequency. However, the frequencies of the $(N-1)$th and Nth difference modes, $\omega_{d(N-1)}$ $(= \omega_s - (N-1)\omega_p)$ and ω_{dN} $(= N\omega_p - \omega_s)$, are lower than ω_p. It will be shown later that the amplitudes of these last two difference modes are governed by coupled integral equations and they can grow faster than exponentially.

In regions $(\text{iii}_{a,b})$ in Figure 5 where $2\alpha_p < \alpha_s < 3\alpha_p$, three difference modes are generated by a $2+3$ mode interaction. A $2 + 4$ mode interaction can occur in regions $(\text{iv}_{a,b})$ where $3\alpha_p < \alpha_s < 4\alpha_p$. For $2 + 3$ mode interactions, the contour lines of constant θ_{d1}, θ_{d2} and θ_{d3} are plotted in regions $(\text{iii}_{a,b})$ in Figure 6. Regions $(\text{iii}_{a,b})$ are located above and below regions $(\text{ii}_{a,b})$ as in Figure 5.

The present analysis will show that the faster-than-exponential growth only occurs to two modes whose frequencies are lower than the primary frequency. They are the secondary and difference modes in a $2 + 1$ mode interaction, and the $(N - 1)$th and Nth difference modes in $2 + N$ mode interactions with $N \ge 2$. When $N \ge 2$, the first $N-1$ quadratic interactions between the primary and secondary/difference modes generates $N - 1$ difference modes whose frequencies are successively decreased by the amount of the primary frequency. The frequency of the $(N - 1)$th-difference mode first becomes lower than the primary frequency. Since the frequency of the Nth-difference mode equals the primary frequency minus the $(N - 1)$th-difference frequency, it is also lower than the primary frequency. The $(N - 1)$th and Nth difference modes are analogous to the secondary and difference modes, respectively, of a $2 + 1$ mode interaction. The critical-layer interaction between the primary wind wave and these two modes enables the latter to grow faster than exponentially, and eventually to grow like the exponential-of-an-exponential. The critical-layer analysis and resulting amplitude equations for $N \ge 2$ will be presented in the following sections.

As shown in Appendix F.2 in Lee (2012), the direct interaction between the plane and oblique wind waves does not produce nonlinear effects outside the critical layer. However, the phase-locked interaction (Wu & Stewart 1996) can occur between the plane wave and nonlinearly generated difference modes whose frequencies are lower than the plane-wave frequency. Additional difference modes are generated by critical-layer interactions between the plane and original difference modes. The frequencies of the original and additional difference modes are lower than the plane wave frequency.

UNSTEADY FLOW OUTSIDE THE CRITICAL LAYER

The unsteady flow in the outer region is composed of a primary and secondary wind wave and N difference modes where N is determined by (15). The difference modes are generated by nonlinear critical-layer interactions. All difference modes as well as the primary and secondary waves have the same wave speed in the streamwise direction, c. The difference modes are assumed not to satisfy the free-surface-wave dispersion relation (11). There are special cases where one of them satisfies (11) as mentioned before.

The analysis in this section closely follows that in §3 in Lee (2012). One important difference is that the secondary wave is linear when $N \geq 2$, although it was nonlinear in Lee (2012) when $N = 1$. The present analysis also includes multiple difference modes. The primary wave is linear in both cases.

Unsteady flow in the water

The velocity potential $\tilde{\phi}$ and pressure perturbation $\tilde{p}_w$ in the water, and the interface surface elevation $\tilde{h}$ can be written as,

$$
\begin{pmatrix} \tilde{\phi} \\ \tilde{p}_w \\ \tilde{h} \end{pmatrix} = \tilde{B}_p \begin{pmatrix} \hat{\phi}_p^{(1)} + \sigma\hat{\phi}_p^{(2)} \\ \hat{p}_p^{(1)} + \sigma\hat{p}_p^{(2)} \\ \hat{h}_p^{(1)} + \sigma\hat{h}_p^{(2)} \end{pmatrix} \mathcal{E}_p + \delta\tilde{B}_s \begin{pmatrix} \hat{\phi}_s^{(1)} + \sigma\hat{\phi}_s^{(2)} \\ \hat{p}_s^{(1)} + \sigma\hat{p}_s^{(2)} \\ \hat{h}_s^{(1)} + \sigma\hat{h}_s^{(2)} \end{pmatrix} \mathcal{E}_s + \sigma\delta \sum_{n=1}^{N} \tilde{B}_{dn} \begin{pmatrix} \hat{\phi}_{dn}^{(2)} \\ \hat{p}_{dn}^{(2)} \\ \hat{h}_{dn}^{(2)} \end{pmatrix} \mathcal{E}_{dn} + c.c. + \dots , \quad (28)
$$

where c.c. denotes the complex conjugate, and

$$
\mathcal{E}_\imath \equiv \exp[\mathrm{i}(\alpha_\imath X + \beta_\imath y)] \quad \text{for} \quad \imath = \{p, s, dN\},
$$
$$
\mathcal{E}_{dn} \equiv \exp[\mathrm{i}(-\alpha_{dn} X - \beta_{dn} y)] \quad \text{if} \quad 1 \leq n \leq N-1, \tag{29}
$$

$$
\alpha_{dn} = n\alpha_p - \alpha_s, \quad \beta_{dn} = n\beta_p - \beta_s, \quad \text{for} \quad 1 \leq n, \tag{30}
$$

$$
X \equiv x - ct, \tag{31}
$$

with X denoting the normalized streamwise coordinate in a reference frame moving with the common c.

The subscripts p, s and dn denote the primary, secondary and nth-difference modes, respectively. The streamwise wavenumbers, α_p, α_s, $-\alpha_{d1}$, …, $-\alpha_{d(N-1)}$, and α_{dN} are positive. But, the spanwise wavenumbers β_p, β_s and β_{dn} can be positive or negative as illustrated in Figures 2–4. As in (12) and (13),

$$
\gamma_{dn} \equiv \sqrt{\alpha_{dn}^2 + \beta_{dn}^2} \quad \text{for} \quad 1 \leq n, \tag{32}
$$

$$
\theta_{dn} = \arctan(\beta_{dn}/\alpha_{dn}), \quad \cos\theta_{dn} = |\alpha_{dn}|/\gamma_{dn}, \quad \sin\theta_{dn} = (\alpha_{dn}/|\alpha_{dn}|)\,\beta_{dn}/\gamma_{dn}, \tag{33}
$$

where $-\pi/2 \leq \theta_{dn} \leq \pi/2$. Since all modes have the same c, their frequencies are proportional to the streamwise wavenumbers,

$$
\{\omega_p, \omega_s, \omega_{dn}\} = \{\alpha_p, \alpha_s, |\alpha_{dn}|\} \times c \quad \text{for} \quad 1 \leq n. \tag{34}
$$

Thus,

$$
\omega_{d1} = \omega_s - \omega_p, \quad \omega_{dN} = N\omega_p - \omega_s, \quad \omega_{dn} = \omega_s - n\omega_p \quad \text{for} \quad 2 \leq n \leq N-1. \tag{35}
$$

From (16), (30) and (34), one may show that, if $N \geq 2$,

$$\omega_{d(N-1)} < \omega_p, \quad \omega_{dN} < \omega_p, \quad \omega_p < \omega_{dn} \quad \text{for} \quad 1 \leq n \leq N - 2. \tag{36}$$

The frequencies of the first $N - 2$ difference modes are higher than the primary-wave frequency. But, those of the last two difference modes, the $(N-1)$th and Nth, are lower than the primary frequency.

The magnitude of the unscaled wave elevation is $O(\epsilon)$ for the primary wind wave and $O(\epsilon\delta)$ for the secondary wave. The scalings of ϵ and δ will be determined later (see (69) and (70)). The difference-mode elevations become $O(\sigma\epsilon\delta)$ in water since we only consider the case where difference modes do not satisfy the relation (11).

Equation (6.5) in Lee (2012) shows that the linear growth rate of a wind wave is of $O(\sigma)$. Thus, the scaling for the slow time t_1 over which the wave growth occurs becomes

$$t_1 \equiv \sigma t. \tag{37}$$

The amplitude functions that account for the slow growth of waves are denoted by $\tilde{B}_i(t_1)$ for $i = \{p, s, dn\}$.

Both leading and second order velocity potentials $\hat{\phi}_i^{(1)}(z)$ and $\hat{\phi}_i^{(2)}(z, t_1)$, for $i = \{p, s, d1, \ldots, dN\}$, satisfy the Laplace equations. The solutions for the primary and secondary waves become,

$$\hat{\phi}_i^{(1)} = \cosh\left[\gamma_i(z + H)\right] / \cosh(\gamma_i H), \quad \hat{\phi}_i^{(2)} = 0, \quad \text{for} \quad i = \{p, s\}, \tag{38}$$

where they are normalized by

$$\hat{\phi}_i^{(1)} + \sigma\hat{\phi}_i^{(2)} = 1 \quad \text{at} \quad z = 0. \tag{39}$$

For the difference modes the solutions are

$$\hat{\phi}_{dn}^{(1)} = 0, \quad \hat{\phi}_{dn}^{(2)} = \tilde{d}_n \cosh[\gamma_{dn}(z + H)]D_{dn}(t_1) / \cosh(\gamma_{dn} H), \tag{40}$$

for $1 \leq n \leq N$, where

$$\tilde{d}_n = \alpha_{dn}^2 c^2 / [\{G\gamma_{dn} \tanh(\gamma_{dn} H) - \alpha_{dn}^2 c^2\}\gamma_{dn} \tanh(\gamma_{dn} H)], \tag{41}$$

and $D_{dn}(t_1)$ is determined by nonlinear critical-layer interactions.

Unsteady flow in the air

Air fluctuations outside the critical layer are also governed by linear equations to the required order of approximation. They are written as, in the limit $\sigma \to 0$,

$$\begin{pmatrix} u - U \\ v \\ w \\ p - P_0 + Gz \end{pmatrix} = \epsilon\tilde{B}_p \begin{pmatrix} \hat{U}_p \\ \hat{V}_p \\ -i\gamma_p\Phi_p \\ \Pi_p \end{pmatrix} \mathcal{E}_p + \epsilon\delta\tilde{B}_s \begin{pmatrix} \hat{U}_s \\ \hat{V}_s \\ -i\gamma_s\Phi_s \\ \Pi_s \end{pmatrix} \mathcal{E}_s + \epsilon\delta\sum_{n=1}^{N}\tilde{B}_{dn} \begin{pmatrix} \hat{U}_{dn} \\ \hat{V}_{dn} \\ -i\gamma_{dn}\Phi_{dn} \\ \Pi_{dn} \end{pmatrix} \mathcal{E}_{dn} + c.c. + \ldots \tag{42}$$

The magnitude of velocity and pressure fluctuations is $O(\epsilon)$ for the primary mode, and $O(\epsilon\delta)$ for the secondary and difference modes in the air. The shape functions $\hat{U}_i(z, t_1)$, $\hat{V}_i(z, t_1)$ and $\Pi_i(z, t_1)$, for $i = \{p, s, d1, \ldots, dN\}$, are related to $\Phi_i(z, t_1)$ by equations (3.14) and (3.15) in Lee (2012).

In this analysis, the nonlinear jump of the streamwise fluctuation velocity across the critical layer occurs at the same order as the linear jump. Therefore, the shape function is expressed as, for $\imath = \{p, s, d1, \ldots, dN\}$,

$$\Phi_\imath(z, t_1) = \Phi_\imath^{(a)}(z) + D_\imath(t_1)\Phi_\imath^{(b)}(z), \tag{43}$$

where $D_\imath(t_1)$ will be determined from the critical-layer solutions, and $\Phi_\imath^{(a)}$ and $\Phi_\imath^{(b)}$ satisfy Rayleigh's stability equations

$$(U - c)\left(\partial_z^2 - \gamma_\imath^2\right)\Phi_\imath^{(a,b)} - U''\Phi_\imath^{(a,b)} = 0 \quad \text{with} \quad \partial_z \equiv \partial/\partial z, \tag{44}$$

subject to

$$\Phi_\imath^{(a)} = (i/\gamma_\imath)\partial_z\hat{\phi}_\imath^{(1)} = i\tanh(\gamma_\imath H) \quad \text{at} \quad z = 0, \quad \Phi_\imath^{(a)} \to 0 \quad \text{as} \quad z \to \infty, \tag{45}$$

$$\Phi_\imath^{(b)} = 0 \quad \text{at} \quad z = 0, \quad \Phi_\imath^{(b)} \to 0 \quad \text{as} \quad z \to \infty. \tag{46}$$

The second shape function $\Phi_\imath^{(b)}$ is the second linearly independent solution of Rayleigh's equation, which can be obtained by the method of variation of parameters as in Reutov (1980), Drazin & Reid (2004) and Lee (2012),

$$\Phi_\imath^{(b)} = J_\imath\Phi_\imath^{(a)} - \begin{cases} 0, & z \geq z_c \\ \Phi_\imath^{(a)}\displaystyle\int_z^{z_c}(\Phi_\imath^{(a)})^{-2}d\xi, & z < z_c \end{cases}, \tag{47}$$

where

$$J_\imath \equiv \int_0^{z_c}(\Phi_\imath^{(a)})^{-2}\,dz. \tag{48}$$

The primary mode remains linear throughout the entire analysis and $D_p = 0$. If $N \geq 2$ or $\omega_p < \omega_s$, the secondary mode also remains linear and $D_s = 0$. All difference modes are assumed not to satisfy the free-surface-wave dispersion relation (11), therefore, $\hat{\phi}_{dn}^{(1)} = \Phi_{dn}^{(a)} = 0$.

The first condition at $z = 0$ in (45) was obtained from the kinematic interface condition and (38) with (39), and could be viewed as normalization conditions of Φ_p and Φ_s for the linear outer solutions of the primary and secondary modes. From (45) and (47), we obtain

$$\partial_z\Phi_\imath^{(b)} = -i/\tanh(\gamma_\imath H) \quad \text{at} \quad z = 0, \tag{49}$$

for $\imath = \{p, s, d1, \ldots, dN\}$. Note that $\Phi_{dn}^{(b)}$ for difference modes are also expressed by the above equation, which can be considered as a normalization condition for Φ_{dn} since $\Phi_{dn}^{(a)} = 0$.

One can obtain a relation that expresses the modal growth rate in terms of $\Phi_\imath^{(a)}$ and $D_\imath(t_1)$. For the primary and secondary modes, $\imath = \{p, s\}$, it is written as

$$\left[2i\gamma_\imath\tilde{B}_\imath'/(\alpha_\imath c\tilde{B}_\imath)\right]\tanh(\gamma_\imath H) + (\hat{b}_\imath^+ - \hat{b}_\imath^-)|b_\imath|^2 U_c''/U_c' + D_\imath(t_1) = R_\imath, \tag{50}$$

where

$$R_\imath = -\fint_0^\infty[|\partial_z\Phi_\imath^{(a)}|^2 + \{\gamma_\imath^2 + U''/(U-c)\}|\Phi_\imath^{(a)}|^2]dz - \gamma_\imath\tanh(\gamma_\imath H) + (U_0'/c)\tanh^2(\gamma_\imath H), \tag{51}$$

$$\fint_0^\infty dz = \lim_{\hat{\epsilon}\to 0}\left[\int_0^{z_c-\hat{\epsilon}}dz + \int_{z_c+\hat{\epsilon}}^\infty dz\right]. \tag{52}$$

17

The prime denotes the differentiation with respect to the relevant argument, i.e. $\tilde{B}'_\imath \equiv d\tilde{B}_\imath/dt_1$, $U'' \equiv d^2U/dz^2$, and

$$U'_0 \equiv U'(z=0), \tag{53}$$

$$c = U_c \equiv U(z=z_c), \quad U'_c \equiv U_z(z=z_c), \quad U''_c \equiv U_{zz}(z=z_c), \tag{54}$$

where $z = z_c$ is the location of the critical level. The $b_\imath$ and $\hat{b}^\pm_\imath$ are determined by

$$b_\imath = \Phi^{(a)}_\imath(z=z_c) = \lim_{z \to z^\pm_c} \Phi^{(a)}_\imath(z), \quad \hat{b}^+_\imath - \hat{b}^-_\imath = \left(U'_c/U''_c/b_\imath\right)[\partial_z\Phi^{(a)}_\imath]^{z^+_c}_{z^-_c}. \tag{55}$$

By matching the outer solution with the critical-layer solution we can show that $\hat{b}^+_\imath - \hat{b}^-_\imath$ equals $i\pi$ as in (86). There is no relation corresponding to (50) for the difference modes since $\Phi^{(a)}_{dn} = 0$ (see Appendix B in Lee 2012). In Appendix A, it is found that

$$J_\imath b_\imath = \lim_{z \to z^\pm_c} \Phi^{(b)}_\imath(z) = -\mathrm{i}|J_\imath b_\imath|, \quad J_\imath = -\mathrm{i}U'_c\mathrm{Re}(b_\imath)/(\pi U''_c|b_\imath|^2 b_\imath), \tag{56}$$

for $\imath = \{p, s, d1, \ldots, dN\}$, where Re denotes the real part of a complex variable. For numerical evaluations of $J_\imath$, the above formula is more convenient than the integral form in (48).

Outer solution expansion about the critical level

The velocity and pressure field near the common critical level is obtained by expanding the outer solutions about $z = z_c$ as

$$u - \left(c + U'_c\tilde{z} + \tfrac{1}{2}U''_c\tilde{z}^2 + \ldots\right) =$$
$$\sum_\imath \epsilon\delta_\imath\tilde{B}_\imath\left[\frac{b_\imath\Omega_\imath}{\cos\theta_\imath}\left\{\frac{\sin^2\theta_\imath}{\tilde{z}} + \frac{U''_c}{U'_c}\left(\ln|\tilde{z}| - \tfrac{1}{2}\sin^2\theta_\imath + \hat{b}^\pm_\imath\right)\right\} + \left\{\begin{matrix}0\\D_\imath/(b_\imath\cos\theta_\imath)\end{matrix}\right\}\right]\mathcal{E}_\imath + c.c. + \ldots, \tag{57}$$

$$v = -\sum_\imath \epsilon\delta_\imath\tilde{B}_\imath b_\imath\Omega_\imath(\sin\theta_\imath)\left[1/\tilde{z} - \tfrac{1}{2}(U''_c/U'_c)\right]\mathcal{E}_\imath + c.c. + \ldots, \tag{58}$$

$$w = -\sum_\imath \epsilon\delta_\imath\mathrm{i}\gamma_\imath\tilde{B}_\imath b_\imath\Omega_\imath\left[1 + (U''_c/U'_c)\tilde{z}\left(\ln|\tilde{z}| + \hat{b}^\pm_\imath - 1\right)\right]\mathcal{E}_\imath + c.c. + \ldots, \tag{59}$$

$$p - P_0 + Gz = \sum_\imath \epsilon\delta_\imath\tilde{B}_\imath b_\imath\Omega_\imath(\cos\theta_\imath)U'_c\mathcal{E}_\imath + c.c. + \ldots, \tag{60}$$

where

$$\tilde{z} \equiv z - z_c, \tag{61}$$

$$\delta_p = 1, \quad \delta_s = \delta_{dn} = \delta, \quad \Omega_p = \Omega_s = 1, \quad \Omega_{dn} = J_{dn}D_{dn}, \quad D_p = D_s = 0, \tag{62}$$

for $1 \le n \le N$. The $\sum_\imath$ denotes the summation of all $2 + N$ modes, i.e.

$$\sum_\imath(\ )_\imath \equiv (\ )_p + (\ )_s + (\ )_{d1} + \ldots + (\ )_{dN}. \tag{63}$$

The last term in braces in (57) becomes 0 if $z > z_c$ and $D_\imath/(b_\imath\cos\theta_\imath)$ if $z < z_c$, and $\hat{b}^\pm_\imath$ becomes $\hat{b}^+_\imath$ and $\hat{b}^-_\imath$ above and below the critical level. The above solution becomes singular at $z = z_c$, therefore, it has to be rescaled in this region.

The streamwise velocity jump across the critical layer from the outer solution becomes,

$$[u]^{\tilde{z}=+\infty}_{\tilde{z}=-\infty} = \sum_\imath \epsilon\delta_\imath\tilde{B}_\imath(\sec\theta_\imath)\left[(U''_c/U'_c)b_\imath\Omega_\imath(\hat{b}^+_\imath - \hat{b}^-_\imath) - D_\imath/b_\imath\right]\mathcal{E}_\imath + c.c. + \ldots. \tag{64}$$

This is matched with the jump from the critical-layer solution to derive amplitude equations.

18

CRITICAL-LAYER EQUATIONS

The thickness of a non-equilibrium critical layer, where the growth term is balanced with the linear convection effect, is of the same order as the small growth rate as shown in Reutov (1980), Goldstein, Durbin & Leib (1987), Goldstein & Hultgren (1988), Lee (2012), and others. Thus, the vertical coordinate in this region is scaled by

$$\tilde{\zeta} = (z - z_c)/\sigma = \tilde{z}/\sigma. \tag{65}$$

Viscous terms will enter the critical-layer momentum equations when the Reynolds number in air is scaled by

$$1/R_a = \sigma^3 \tilde{\lambda}, \tag{66}$$

where $\tilde{\lambda}$ is the viscous parameter and $R_a \equiv U_a \Delta_a / \nu_a$ with ν_a denoting the kinematic viscosity of air.

The continuity and momentum equations for the velocity $\boldsymbol{u} = \boldsymbol{i}u + \boldsymbol{j}v + \boldsymbol{k}w$ and pressure p expressed in terms of the scaled variables t_1, X and $\tilde{\zeta}$ become

$$u_X + v_y + w_{\tilde{\zeta}}/\sigma = 0, \tag{67}$$

$$\left[\sigma \frac{\partial}{\partial t_1} + (u - c) \frac{\partial}{\partial X} + v \frac{\partial}{\partial y} + \frac{w}{\sigma} \frac{\partial}{\partial \tilde{\zeta}} - \sigma \tilde{\lambda} \frac{\partial^2}{\partial \tilde{\zeta}^2} \right] \{u, v, w\} = - \left\{ p_X, p_y, G + \frac{1}{\sigma} p_{\tilde{\zeta}} \right\}. \tag{68}$$

The magnitude of a difference mode in air, that is generated by a quadratic interaction between a primary wave and a secondary or other difference mode, becomes of the same order as the secondary amplitude when

$$\epsilon = \sigma^3. \tag{69}$$

Meanwhile, the nonlinear effect due to the quadratic coupling of the secondary and 1st-difference modes, or of a pair of difference modes, becomes negligibly small when δ, which is a measure of the amplitude ratio of the secondary to primary modes, satisfies

$$\delta \ll 1. \tag{70}$$

Introducing (65) and (69) into the outer solutions (57)–(60) and re-expanding the result for small $\tilde{\zeta}$ show that the critical-layer solution should be of the form

$$\begin{pmatrix} u \\ v \\ w \\ p \end{pmatrix} = \begin{pmatrix} c + \sigma U_c' \tilde{\zeta} \\ 0 \\ 0 \\ P_0 - Gz \end{pmatrix} + \sigma^2 \begin{pmatrix} u^{(1)} \\ v^{(1)} \\ \sigma w^{(1)} \\ \sigma p^{(1)} \end{pmatrix} + \sigma^3 \ln \sigma \begin{pmatrix} u^{(2L)} \\ v^{(2L)} \\ \sigma w^{(2L)} \\ \sigma p^{(2L)} \end{pmatrix} + \sigma^3 \begin{pmatrix} u^{(2)} \\ v^{(2)} \\ \sigma w^{(2)} \\ \sigma p^{(2)} \end{pmatrix} + \dots. \tag{71}$$

It is convenient to introduce the critical-layer amplitude $\tilde{A}_\imath$,

$$\tilde{A}_\imath = b_\imath \Omega_\imath \tilde{B}_\imath \quad \text{for} \quad \imath = \{p, s, dN\}, \qquad \tilde{A}_{dn} = -b_{dn}^* \Omega_{dn}^* \tilde{B}_{dn}^* \quad \text{for} \quad 1 \leq n \leq N-1, \tag{72}$$

where $\tilde{B}_\imath$ is the amplitude in the outer solutions, and $\Omega_\imath$ is defined by (62). Then, the leading-order term that matches onto the outer solution (57)–(60) is written as

$$\begin{pmatrix} u^{(1)} - \frac{1}{2} U_c'' \tilde{\zeta}^2 \\ v^{(1)} \end{pmatrix} = \mathrm{i} \begin{pmatrix} \beta_p/\alpha_p \\ -1 \end{pmatrix} \tilde{Q}_p^{(1)} \mathcal{E}_p + \delta \mathrm{i} \begin{pmatrix} \beta_s/\alpha_s \\ -1 \end{pmatrix} \tilde{Q}_s^{(1)} \mathcal{E}_s + \delta \mathrm{i} \sum_{n=1}^{N} \begin{pmatrix} \beta_{dn}/\alpha_{dn} \\ -1 \end{pmatrix} \tilde{Q}_{dn}^{(1)} \tilde{\mathcal{E}}_{dn} + c.c., \tag{73}$$

19

$$
\begin{pmatrix} w^{(1)} \\ p^{(1)} \end{pmatrix} = \begin{pmatrix} -i\gamma_p \\ U'_c\alpha_p/\gamma_p \end{pmatrix} \tilde{A}_p\mathcal{E}_p + \delta \begin{pmatrix} -i\gamma_s \\ U'_c\alpha_s/\gamma_s \end{pmatrix} \tilde{A}_s\mathcal{E}_s + \delta \sum_{n=1}^{N} \begin{pmatrix} -i\gamma_{dn} \\ U'_c\alpha_{dn}/\gamma_{dn} \end{pmatrix} \tilde{A}_{dn}\tilde{\mathcal{E}}_{dn} + c.c.. \tag{74}
$$

The wavenumbers are defined by (12), (30) and (32). The $\mathcal{E}_p$ and $\mathcal{E}_s$ are given in (29), and $\tilde{\mathcal{E}}_{dn}$ is defined as

$$
\tilde{\mathcal{E}}_{dn} \equiv \exp[i(\alpha_{dn}X + \beta_{dn}y)] \quad \text{for} \quad 1 \le n, \tag{75}
$$

that becomes $\tilde{\mathcal{E}}_{dn} = \mathcal{E}_{dn}^*$ if $1 \le n \le N-1$, and $\tilde{\mathcal{E}}_{dN} = \mathcal{E}_{dN}$ with $\mathcal{E}_{dn}$ given in (29). The second-order critical-layer solution must include all harmonics generated by the nonlinear terms in the momentum equations. They become, up to $O(\delta)$,

$$
q^{(2)} = \tilde{Q}_p^{(2)}\mathcal{E}_p + \tilde{Q}_0^{(2)} + \tilde{Q}_{2p}^{(2)}\mathcal{E}_p^2 + \delta \left[\tilde{Q}_s^{(2)}\mathcal{E}_s + \tilde{Q}_{p+s}^{(2)}\mathcal{E}_p\mathcal{E}_s + \sum_{n=1}^{N+1} \tilde{Q}_{dn}^{(2)}\tilde{\mathcal{E}}_{dn} \right] + c.c., \tag{76}
$$

where $q^{(2)}$ and $\tilde{Q}_j^{(2)}$ denote

$$
q^{(2)} \equiv \left\{ u^{(2)} - \tfrac{1}{6}U_c'''\tilde{\zeta}^3, \ v^{(2)}, \ w^{(2)}, \ p^{(2)} \right\}, \tag{77}
$$

$$
\tilde{Q}_j^{(2)} \equiv \left\{ \tilde{U}_j^{(2)}, \ \tilde{V}_j^{(2)}, \ \tilde{W}_j^{(2)}, \ \tilde{P}_j^{(2)} \right\} \quad \text{for} \quad j = \{p, \ 0, \ 2p, \ s, \ p+s, \ d1, \ \dots, \ d(N{+}1)\}. \tag{78}
$$

By substituting (71), (73), (74) and (76)–(78) into the continuity and momentum equations, a system of critical-layer equations is derived for $\tilde{Q}_i^{(1)}$ and $\tilde{Q}_j^{(2)}$ as given in Appendix B.

AMPLITUDE EQUATIONS

Matching of critical-layer jumps

The critical-layer equations in Appendix B are analytically solved to obtain the velocity jumps across the critical layer as in Goldstein & Choi (1989), Goldstein & Lee (1992), Wu (1992), Wu, Lee & Cowley (1993), Lee (2012), and others. The following normalized variables are introduced,

$$\hat{\alpha}_\imath = \alpha_\imath/\bar{\alpha}, \quad \hat{\beta}_\imath = \beta_\imath/\bar{\beta}, \quad \hat{\gamma}_\imath = \gamma_\imath/\bar{\beta}, \tag{79}$$

$$\bar{t} = \hat{\kappa}(\bar{\alpha}U_c't_1 - t_o), \quad \zeta = \tilde{\zeta}/\hat{\kappa} - \tilde{\zeta}_o, \quad \bar{X} = X - X_o, \quad \lambda = \tilde{\lambda}/(\bar{\alpha}\hat{\kappa}^3 U_c'), \tag{80}$$

$$A_\imath = (\sqrt{M/U_c'}/\hat{\kappa}^3)\tilde{A}_\imath \, e^{i\hat{\alpha}_\imath(X_o + \tilde{\zeta}_o\bar{t})}, \quad U_j^{(2)} = \{\bar{\alpha}^2 M/(\bar{\beta}^2\hat{\kappa}^3)\}\, \tilde{U}_j^{(2)} \, e^{i\hat{\alpha}_\jmath(X_o + \tilde{\zeta}_o\bar{t})}, \tag{81}$$

where the normalization parameters $\bar{\alpha}$, $\bar{\beta}$, $\hat{\kappa}$ and M and the coordinate origin shift $\tilde{\zeta}_o$ are chosen in Appendix C, and t_o and X_o will be chosen later.

When $N \geq 2$, the velocity jumps of the primary, secondary and N difference modes become

$$\int_{-\infty}^{\infty} U_{\jmath\zeta}^{(2)}d\zeta = i\pi(\bar{\alpha}/\bar{\beta})\sqrt{M/U_c'}\, U_c''(\hat{\gamma}_\jmath/\hat{\alpha}_\jmath)\, A_\jmath(\bar{t}) \quad \text{for} \quad \jmath = \{p, s\}, \tag{82}$$

$$\int_{-\infty}^{\infty} U_{dn\,\zeta}^{(2)}d\zeta = \begin{cases} \Lambda_n^- + F_n^-, & 1 \leq n \leq N-2, \\ \Lambda_n^- + F_n^- + G_n^+, & n = N-1, \\ \Lambda_n^+ + G_n^-, & n = N, \end{cases} \tag{83}$$

where $\Lambda_n^\pm$, F_n^- and $G_n^\pm$ are given in Appendix D.

The difference mode jumps (83) are rewritten as, for example, if $N = 2$,

$$\int_{-\infty}^{\infty} U_{dn\,\zeta}^{(2)}d\zeta = \begin{cases} \Lambda_1^-(\bar{t}|A_{d1}) + F_1^-(\bar{t}|A_p, A_s^*) + G_1^+(\bar{t}|A_p^*, A_{d2}), & n = 1, \\ \Lambda_2^+(\bar{t}|A_{d2}) + G_2^-(\bar{t}|A_p, A_{d1}), & n = 2. \end{cases} \tag{84}$$

Two difference modes are generated by a $2 + 2$ mode interaction as shown in Figures 2(e, f)–4(e, f). When $N = 3$, equation (83) for a $2 + 3$ mode interaction becomes

$$\int_{-\infty}^{\infty} U_{dn\,\zeta}^{(2)}d\zeta = \begin{cases} \Lambda_1^-(\bar{t}|A_{d1}) + F_1^-(\bar{t}|A_p, A_s^*), & n = 1, \\ \Lambda_2^-(\bar{t}|A_{d2}) + F_2^-(\bar{t}|A_p, A_{d1}) + G_2^+(\bar{t}|A_p^*, A_{d3}), & n = 2, \\ \Lambda_3^+(\bar{t}|A_{d3}) + G_3^-(\bar{t}|A_p, A_{d2}), & n = 3. \end{cases} \tag{85}$$

Diagrams of $2 + 3$ mode interactions are illustrated in Figures 2(g, h)–4(g, h).

Matching between the critical-layer solutions (71) and the outer solutions (57)–(60) requires that the velocity jumps (82) and (83) from the critical-layer solutions at $O(\sigma^3\delta_\imath)$ must be equal to the corresponding velocity jumps (64) from the outer solution. By matching them, we obtain

$$\hat{b}_\imath^+ - \hat{b}_\imath^- = i\pi, \tag{86}$$

21

$$D_p = D_s = 0, \quad D_{dn}B_{dn} = -\left[\bar{\beta}b_{dn}\hat{\alpha}_{dn}/(\bar{\alpha}\hat{\gamma}_{dn}\sqrt{U_c'M})\right]F_{dn}(\bar{t}) \text{ for } 1 \leq n \leq N, \quad (87)$$

where F_{dn} denotes the nonlinear jumps without the $\Lambda_n^{\pm}$ terms on the right sides of (83). The normalized outer amplitude $B_\imath$ is related to the normalized critical-layer amplitude $A_\imath$ by

$$A_\imath = b_\imath\Omega_\imath B_\imath \quad \text{with} \quad B_\imath = (\sqrt{M/U_c'}/\hat{\kappa}^3)\tilde{B}_\imath e^{i\hat{\alpha}_\imath(X_o+\tilde{\zeta}_o\bar{t})}. \quad (88)$$

The above equations (86)–(88) with the relation (50) completely determine the evolution of amplitudes. They can be combined to derive more explicit amplitude equations as will be summarized below.

Primary and secondary mode amplitudes

The primary mode, whose magnitude of $O(\sigma^3)$ is larger than the other modes, remains linear throughout the whole stage. When $N \geq 2$, or $\omega_p < \omega_s$, the secondary mode of magnitude of $O(\sigma^3\delta)$ also remains linear. From the relation (50) and the matching conditions (86) and (87), we can show that

$$A_p = a_p\exp(\kappa_p\bar{t}), \quad A_s = a_s\exp(\kappa_s\bar{t}). \quad (89)$$

The linear growth rates κ_p and κ_s become

$$\kappa_\imath = -\frac{\pi c U_c''\hat{\alpha}_\imath|b_\imath|^2}{2\hat{\kappa}\bar{\beta}U_c'^2\hat{\gamma}_\imath\tanh(\gamma_\imath H)} - i\hat{\alpha}_\imath\left(\frac{cR_\imath}{2\hat{\kappa}\bar{\beta}U_c'\hat{\gamma}_\imath\tanh(\gamma_\imath H)} - \tilde{\zeta}_o\right) \quad \text{for} \quad \imath = \{p, s\}, \quad (90)$$

with $\bar{\beta}$, $\hat{\kappa}$, $\tilde{\zeta}_o$ and $R_\imath$ in (C-1)–(C-3) and (51). The initial amplitudes a_p and a_s are

$$a_\imath = (\tilde{A}_\imath^{(o)}/\tilde{A}_{30}^{(o)})\exp\left[(\kappa_\imath - 1)\hat{\kappa}t_o + i(\hat{\alpha}_\imath - \hat{\alpha}_{30})(X_o - \hat{\kappa}t_o\tilde{\zeta}_o)\right] \quad \text{for} \quad \imath = \{p, s\}, \quad (91)$$

where $\tilde{A}_\imath^{(o)}$ is a non-normalized initial amplitude of $\tilde{A}_\imath$,

$$\tilde{A}_\imath = \tilde{A}_\imath^{(o)}e^{\tilde{\kappa}_\imath t_1}, \quad (92)$$

and $\tilde{\kappa}_\imath$ is the non-normalized linear growth rate,

$$\tilde{\kappa}_\imath = (d\tilde{A}_\imath/dt_1)/\tilde{A}_\imath = \bar{\alpha}\hat{\kappa}U_c'(\kappa_\imath - i\hat{\alpha}_\imath\tilde{\zeta}_o). \quad (93)$$

The coordinate origin shifts t_o and X_o introduced in (80) are chosen to satisfy

$$(\sqrt{M/U_c'}/\hat{\kappa}^3)\tilde{A}_{30}^{(o)}\exp\left[\hat{\kappa}t_o + i\hat{\alpha}_{30}(X_o - \hat{\kappa}t_o\tilde{\zeta}_o)\right] = 1. \quad (94)$$

By putting (C-2) and (C-3) into (90), and from (91),

$$\kappa_{30} = 1, \quad a_{30} = 1. \quad (95)$$

In Lee (2012), we showed that κ_p and a_p could be normalized to unity by selecting the properties of the primary and secondary waves of each set of interactions as normalization parameters. The a_s could also be normalized to be one. However, in this paper, the general forms in (89), with normalization parameters chosen from the properties of a wind wave with 30° propagation angle will be kept for straightforward comparisons between numerical results of various sets of interactions.

When the secondary-wave frequency is lower than the primary frequency, or $N = 1$, the $2+1$ mode interaction produces a nonlinear effect on the secondary wind wave. Its amplitude is then governed by an integro-differential equation.

Amplitude equations of difference modes when $\lambda = O(1)$

Equation (87) shows that the amplitudes of the first $N - 2$ difference modes grow exponentially,

$$A_{dn} = a_{dn}\exp(\kappa_{dn}\bar{t}) \quad \text{for} \quad 1 \le n \le N-2. \tag{96}$$

Their growth rates, κ_{dn}, and initial amplitudes, a_{dn}, become

$$\kappa_{dn} = \kappa_s^* + n\kappa_p, \tag{97}$$

$$a_{dn} = \varphi_{dn}^* a_p a_{d(n-1)} I_d^{(n)} \quad \text{with} \quad a_{d0} = -a_s^*, \tag{98}$$

where φ_{dn} and $I_d^{(n)}$ are given by

$$\varphi_{dn} = -\frac{\hat{\gamma}_{30}\hat{\alpha}_{dn}}{\hat{\alpha}_{30}\hat{\gamma}_{dn}}\frac{J_{dn}b_{dn}^2}{|J_{30}||b_{30}|^2} = \mathrm{i}\frac{b_{dn}}{|b_{dn}|}\frac{\hat{\gamma}_{30}\hat{\alpha}_{dn}}{\hat{\alpha}_{30}\hat{\gamma}_{dn}}\frac{|J_{dn}||b_{dn}|^2}{|J_{30}||b_{30}|^2}, \tag{99}$$

$$I_d^{(n)} = C_{c-}^{(n)}\left[\nu_n\hat{\gamma}_{d(n-1)}\int_0^\infty E_{a-}^{(n)}(\tau)\,\mathrm{e}^{-(\hat{\nu}\kappa_p+\kappa_s^*)\tau}\,\tau^2\,d\tau\right.$$
$$\left. -C_{d-}^{(n)}\int_0^\infty\int_0^\infty E_{u-}^{(n)}(\tau_1,\tau_2)\,\mathrm{e}^{-(\hat{\nu}\kappa_p+\kappa_s^*)(\tau_1+\tau_2)}\,\tau_1\,d\tau_1 d\tau_2\right], \tag{100}$$

with $\hat{\nu}$, ν_n, $C_{c-}^{(n)}$, $C_{d-}^{(n)}$, $E_{a-}^{(n)}$ and $E_{u-}^{(n)}$ in (D-4)–(D-7). The relation (56) was used to obtain (99).

However, the amplitudes of the last two difference modes, the $(N-1)$th and Nth, are determined by coupled integral equations

$$A_{d(N-1)} = a_{d(N-1)}\exp(\kappa_{d(N-1)}\bar{t}) + \varphi_{d(N-1)}^* G_{N-1}^+(\bar{t}|A_p^*, A_{dN}), \tag{101}$$

$$A_{dN} = -\varphi_{dN}G_N^-(\bar{t}|A_p, A_{d(N-1)}), \tag{102}$$

with $a_{d(N-1)}$ defined by (98) and $G_n^{\pm}$ given by (D-3) in Appendix D. The above equations determine $A_{d(N-1)}$ and A_{dN} at a given $\bar{t}$.

From (101) and (102), one may obtain that

$$A_{d(N-1)} \to a_{d(N-1)}\exp(\kappa_{d(N-1)}\bar{t}), \quad A_{dN} \to a_{dN}\exp(\kappa_{dN}\bar{t}), \quad \text{as} \quad \bar{t} \to -\infty, \tag{103}$$

where $\kappa_{d(N-1)}$, κ_{dN} and $a_{d(N-1)}$ are defined by (97) and (98), and a_{dN} is equal to r_0 in (125).

Equations (36) and (96) show that the first $N-2$ difference modes, whose frequencies are higher than the primary-wave frequency, grow exponentially. The growth rate of the nth-difference mode is increased by κ_p and its frequency is decreased by ω_p compared to those of the preceding $(n-1)$th-difference mode. As shown in (103) and (115), the growth rates of the $(N-1)$th and Nth difference modes in the initial exponential-growth stage are also larger by κ_p than the $(N-2)$th and $(N-1)$th modes, respectively. However, the growth rates of these last two difference modes can become much greater than their initial growth rates when $\bar{t}$ becomes large. The frequencies of the $(N-1)$th and Nth difference modes are lower than the primary frequency as given in (36).

The amplitudes of all $2 + N$ modes ($N \ge 2$) are now determined by (89), (96), (101) and (102). It is noted that only initial amplitudes of the wind waves, a_p and a_s, can be freely chosen as in (89). All initial amplitudes of nonlinearly generated difference modes, a_{dn}, are determined by (98). The governing equations become much simpler in the inviscid and large-viscosity limits as will be given later. We will also obtain the series solutions of the $(N-1)$th and Nth difference-mode amplitude equations.

23

Outer amplitudes B_p, B_s and B_{dn}

From (62), (87) and (88), the primary and secondary amplitudes in the outer solutions, B_p and B_s, that are normalized by the second equation in (88), become

$$B_p = A_p/b_p, \qquad B_s = A_s/b_s, \tag{104}$$

where A_p and A_s are given by (89). The difference mode is solely generated by the critical-layer interaction, and B_{dn} always appears multiplied by D_{dn} in the outer solution (57)–(60). From (88) with (62), the term $D_{dn}B_{dn}$ becomes

$$D_{dn}B_{dn} = A_{dn}/(b_{dn}J_{dn}). \tag{105}$$

The outer solutions in the air, the perturbations in the water and the wave elevation are now completely determined.

INVISCID AMPLITUDE EQUATIONS

In the inviscid limit where $\lambda = 0$, (96) becomes

$$A_{dn} = a_{dn}^{(inv)}\exp(\kappa_{dn}\bar{t}) \quad \text{for} \quad 1 \leq n \leq N-2, \tag{106}$$

with

$$a_{dn}^{(inv)} = \varphi_{dn}^* a_p a_{d(n-1)}^{(inv)} I_{d_{inv}}^{(n)}, \tag{107}$$

$$I_{d_{inv}}^{(n)} = I_d^{(n)}(\lambda = 0) = C_{c-}^{(n)}\left(2\nu_n\hat{\gamma}_{d(n-1)} - C_{d-}^{(n)}\right)/\left(\hat{\nu}\kappa_p + \kappa_s^*\right)^3. \tag{108}$$

Equations (101) and (102) are simplified as

$$A_{d(N-1)} = a_{d(N-1)}^{(inv)}\exp(\kappa_{d(N-1)}\bar{t}) + \hat{\varphi}_a^{(inv)}\,\mathrm{e}^{2(\mathrm{Re}\kappa_p)\bar{t}} \int_0^\infty K_d^{(inv)}(\tau)\,A_{d(N-1)}(\bar{t} - \tau)d\tau, \tag{109}$$

$$A_{dN} = \hat{\varphi}_b^{(inv)}\,\mathrm{e}^{\kappa_p\bar{t}} \int_0^\infty \mathrm{e}^{-(1-\nu_N)\kappa_p\tau}\,\tau^2\,A_{d(N-1)}(\bar{t} - \tau)d\tau, \tag{110}$$

where

$$K_d^{(inv)} = \mathrm{e}^{-(1-\nu_N)\kappa_p\tau}\left[\tau^2 - 3\tau/(\nu_N\mathrm{Re}\kappa_p) + 3/(\nu_N\mathrm{Re}\kappa_p)^2\right]$$
$$-\mathrm{e}^{-(\kappa_p+\nu_N\kappa_p^*)\tau}\left[\tau^2 + 3\tau/(\nu_N\mathrm{Re}\kappa_p) + 3/(\nu_N\mathrm{Re}\kappa_p)^2\right], \tag{111}$$

$$\hat{\varphi}_a^{(inv)} = -\tfrac{1}{4}|a_p|^2\varphi_{d(N-1)}^* C_{a+}^{(N-1)}\left(\nu_{N-1}\hat{\gamma}_p - \tfrac{1}{2}C_{b+}^{(N-1)}\right)\hat{\varphi}_b^{(inv)}/(\nu_N\mathrm{Re}\kappa_p)^3, \tag{112}$$

$$\hat{\varphi}_b^{(inv)} = -a_p\varphi_{dN} C_{a-}^{(N)}\left(\nu_N\hat{\gamma}_p - \tfrac{1}{2}C_{b-}^{(N)}\right). \tag{113}$$

From (D-4) and (16),

$$\nu_N = N - \hat{\nu} = N - \hat{\alpha}_s/\hat{\alpha}_p \quad \text{and} \quad 0 < \nu_N < 1. \tag{114}$$

Equations (89), (106), (109) and (110) determine the inviscid amplitudes. The series solutions of (109) and (110) will be given later. We will also find the conditions when the coefficients $\hat{\varphi}_a^{(inv)}$ and $\hat{\varphi}_b^{(inv)}$ vanish.

The amplitudes $A_{d(N-1)}$ and A_{dN} in (109) and (110) become

$$A_{d(N-1)} \to a_{d(N-1)}^{(inv)}\exp(\kappa_{d(N-1)}\bar{t}), \quad A_{dN} \to a_{dN}^{(inv)}\exp(\kappa_{dN}\bar{t}), \quad \text{as} \quad \bar{t} \to -\infty, \tag{115}$$

where $a_{d(N-1)}^{(inv)}$ is given by (107), and $a_{dN}^{(inv)}$ equals r_0 defined later by (125).

25

SOLUTIONS OF VISCOUS-LIMIT AMPLITUDE EQUATIONS

In the large-viscosity limit where $\lambda \to \infty$, (96) can be written as

$$A_{dn} = a_{dn}^{(vlim)} \exp(\kappa_{dn}\bar{t}) \quad \text{for} \quad 1 \leq n \leq N-2, \tag{116}$$

where

$$a_{dn}^{(vlim)} = \varphi_{dn}^* a_{d(n-1)}^{(vlim)} I_{d_{vlim}}^{(n)}, \tag{117}$$

$$I_{d_{vlim}}^{(n)} = \lim_{\lambda \to \infty} I_d^{(n)} = C_{c-}^{(n)} \left[\hat{\gamma}_{d(n-1)} / \{\lambda\hat{\alpha}_p^2 \nu_n (1-\nu_n)\} - C_{d-}^{(n)} \int_0^\infty \int_0^\infty E_{u-}^{(n)}(\tau_1,\tau_2)\,\tau_1 d\tau_1 d\tau_2 \right]. \tag{118}$$

The viscous-limit amplitude equations for the $(N-1)$th and Nth difference modes are obtained by taking the $\lambda \to \infty$ limits of (101) and (102) using similar methods in Wu *et al.* (1993) and Lee (2012). These equations are solved to obtain the following analytic solutions

$$A_{d(N-1)} = a_{d(N-1)}^{(vlim)} \exp(\kappa_{d(N-1)}\bar{t}) / (1 - \hat{\varphi}_a^{(vlim)}\,\mathrm{e}^{2(\mathrm{Re}\kappa_p)\bar{t}}), \quad A_{dN} = \hat{\varphi}_b^{(vlim)}\,\mathrm{e}^{\kappa_p\bar{t}}\,A_{d(N-1)}, \tag{119}$$

where

$$\hat{\varphi}_a^{(vlim)} = |a_p|^2 \varphi_{d(N-1)}^* \hat{\varphi}_b^{(vlim)} \tilde{G}_{N-1}^+, \quad \hat{\varphi}_b^{(vlim)} = -a_p\varphi_{dN}\tilde{G}_N^-, \tag{120}$$

$$\tilde{G}_{N-1}^\pm = \mp C_{a\pm}(n) \left[\hat{\gamma}_p / \{\lambda\hat{\alpha}_p^2 \nu_n (1 \pm \nu_n)^2\} - C_{b\pm}^{(n)} \int_0^\infty \int_0^\infty E_{v\pm}^{(n)}(\tau_1,\tau_2)\,\tau_1\,d\tau_1 d\tau_2 \right]. \tag{121}$$

By renormalizing the amplitudes and time, we may find that λ is not an independent parameter for the above solutions. In the large-viscosity limit, the evolution of all amplitudes is described by simple algebraic equations (89), (116) and (119).

SERIES SOLUTIONS OF AMPLITUDE EQUATIONS

Both inviscid and finite-viscosity amplitude equations, in (101), (102), (109) and (110), possess the following absolutely-convergent series solutions,

$$A_{d(N-1)} = \sum_{n=0}^{\infty} s_n \exp[(2n\mathrm{Re}\kappa_p + \kappa_{d(N-1)})\,\bar{t}], \quad A_{dN} = \sum_{n=0}^{\infty} r_n \exp[(2n\mathrm{Re}\kappa_p + \kappa_{dN})\,\bar{t}], \tag{122}$$

where κ_{dn} is defined by (97). The recursion relations are obtained as

$$s_0 = a_{d(N-1)}^{(inv)} \quad \text{if} \quad \lambda = 0, \qquad s_0 = a_{d(N-1)} \quad \text{if} \quad \lambda \neq 0, \tag{123}$$

$$s_n = (1/4)\hat{\varphi}_a^{(inv)}\nu_N^3(n-1+\xi)^{-3}(n-1+\xi+\nu_N)^{-3}(\mathrm{Re}\kappa_p)^{-3}\,g_{n-1}\,s_{n-1} \quad \text{for} \quad n \geq 1, \tag{124}$$

$$r_n = (1/4)\hat{\varphi}_b^{(inv)}(n+\xi)^{-3}(\mathrm{Re}\kappa_p)^{-3}\,h_n\,s_n \quad \text{for} \quad n \geq 0, \tag{125}$$

where

$$\xi \equiv (\hat{\nu}\kappa_p + \kappa_s^*)/(2\mathrm{Re}\kappa_p). \tag{126}$$

In the inviscid limit, g_{n-1} and h_n become

$$g_{n-1} = h_n = 1 \quad \text{if} \quad \lambda = 0, \tag{127}$$

and they are given by (E-1) and (E-2) in Appendix E for the finite-viscosity case.

The recursion relation (124) is summed to obtain

$$s_n = \left(\hat{\varphi}_a^{(inv)}/4\right)^n (\nu_N/\mathrm{Re}\kappa_p)^{3n}\,[(\xi)_n(\xi+\nu_N)_n]^{-3}\left(\prod_{m=1}^{n} g_{m-1}\right) s_0, \tag{128}$$

where $(\xi)_n \equiv \Gamma(\xi+n)/\Gamma(\xi)$ denotes the generalized factorial function, and $\Gamma(\xi)$ is the gamma function.

Following the method used in Wundrow, Hultgren & Goldstein (1994), we can show that the asymptotic behavior of (122) when $\bar{t} \to \infty$ becomes

$$A_{d(N-1)}(\bar{t}) \sim s_{asy}\exp\left[\left\{\kappa_{d(N-1)} - (2\xi + \nu_N - 7/6)\mathrm{Re}\kappa_p\right\}\bar{t}\right]$$
$$\times \exp\left[6\left\{(\nu_N/\mathrm{Re}\kappa_p)^3\hat{\varphi}_a^{(inv)}/4\right\}^{1/6}\exp\{(\mathrm{Re}\kappa_p/3)\bar{t}\}\right], \tag{129}$$

$$A_{dN}(\bar{t}) \sim r_{asy}\exp\left[\mathrm{i}(\mathrm{Im}\kappa_p)\bar{t}\right] A_{d(N-1)}(\bar{t}), \tag{130}$$

where s_{asy} and r_{asy} are given in (E-7) and (E-8), and Im denotes the imaginary part of a complex variable.

Similar to previous analyses by Goldstein & Lee (1992), Wundrow *et al.* (1994) and Lee (2012), the amplitudes $A_{d(N-1)}$ and A_{dN} grow like the exponential-of-an-exponential as $\bar{t} \to \infty$. It is worth noting that the viscous effect only appears in the coefficients s_{asy} and r_{asy} in (129) and (130). Their $\bar{t}$-dependent parts, or $A_{d(N-1)}/s_{asy}$ and A_{dN}/r_{asy}, are independent of λ.

SPECIAL SOLUTIONS OF AMPLITUDE EQUATIONS

Generation of plane second-difference modes by $2 + 2$ mode interactions

By putting $\beta_{dn} = 0$ and using (11), (12) and (30), we may show that a $2 + 2$ mode interaction can generate a second-difference mode whose motion is two-dimensional, or $\theta_{d2} = 0$, if α_p and α_s satisfy

$$\alpha_s^2 = \left(1 + \sqrt{1 + 16m_s(m_p\alpha_p^2 - 1)\alpha_p^2}\right)/(2m_s), \tag{131}$$

where $m_\imath = c^4/[G^2\tanh^2(\gamma_\imath H)]$ for $\imath = \{p, s\}$. The combinations of (θ_p, θ_s) that satisfy (131) are plotted as the $\theta_{d2} = 0$ contour line in Figure 6(b) and also as red curves in Figures 7(a, b).

One can further show that the plane 2nd-difference mode is a wind wave, if

$$(4 - m_p/m_s)\bar{r}^2\bar{v}_p^4 - 8\bar{r}\bar{v}_p^3 + 6\bar{v}_p^2 + (1 - 2/\bar{r}^2)\bar{r}\bar{v}_p + (1/\bar{r}^2 - 1)/4 = 0, \tag{132}$$

where $\bar{v}_p \equiv \sqrt{m_s}\alpha_p$, $\bar{r} \equiv \tanh(\gamma_s H)/\tanh(\alpha_{2D} H)$ and $\alpha_{2D} = (G/c^2)\tanh(\alpha_{2D} H)$. In the deep water limit, where $\tanh(\gamma_\imath H) \to 1$ and $\tanh(\alpha_{2D} H) \to 1$, (132) becomes

$$\alpha_p = (5 + \sqrt{13})G/(6c^2). \tag{133}$$

With parameter values in (14) and (134), the condition is satisfied by the primary and secondary waves with $\theta_p \approx 45.8°$ and $\theta_s \approx 57.6°$. The above results (131)–(133) are independent of λ.

If the plane 2nd-difference mode is not a wind wave, the amplitudes of both difference modes, A_{d1} and A_{d2}, grow exponentially and they are determined by (103) or (115) with $N = 2$. When the condition (132) or (133) is satisfied, A_{d2} will be determined by an equation that is similar to (5.12) in Lee (2012).

When $\alpha_s = N\alpha_p$

If $\alpha_s = N\alpha_p$, the critical-layer interaction generates N difference modes with wavenumbers given by (30). Since the streamwise wavenumber of the Nth-difference mode is zero, its outer solution is not singular and, as a result, the difference-mode or nonlinear-effect generation mechanism is stopped. If $N = 1$ and $\beta_s = \beta_p$, the Nth-difference mode becomes trivial for the primary oblique wave interacting with itself (Goldstein & Leib 1989). In other cases, i.e. if $N = 1$ and $\beta_s = -\beta_p$, or if $N \geq 2$, the Nth-difference mode becomes steady and spanwise periodic (Goldstein & Choi 1989). The exponentially-growing amplitudes of the first $N - 1$ difference modes are determined by (96) and (103). When $N = 0$, the plane secondary wave grows exponentially, but the difference mode is not generated as given in Appendix F.2 in Lee (2012).

When $\hat{\varphi}_a^{(inv)} = 0$ and $\hat{\varphi}_b^{(inv)} = 0$

The coefficients $\hat{\varphi}_a^{(inv)}$ and $\hat{\varphi}_b^{(inv)}$ in the inviscid amplitude equations (109) and (110) can become zero. In Figure 7(a), the combinations of (θ_p, θ_s) for $\hat{\varphi}_a^{(inv)} = 0$ are plotted. The contour lines of $\hat{\varphi}_b^{(inv)} = 0$ are plotted in Figure 7(b) for the parameter values in (14) and (134). Border lines for various $2 + N$ mode interactions, which were shown in Figure 5, are replotted for $1 \leq N \leq 7$ as green dotted curves. The red solid curve depicts the (θ_p, θ_s) combinations that generate plane second-difference modes. It is the same curve as the $\theta_{d2} = 0$ contour line in Figure 6(b). Because of (112), $\hat{\varphi}_a^{(inv)} = 0$ if $\hat{\varphi}_b^{(inv)} = 0$.
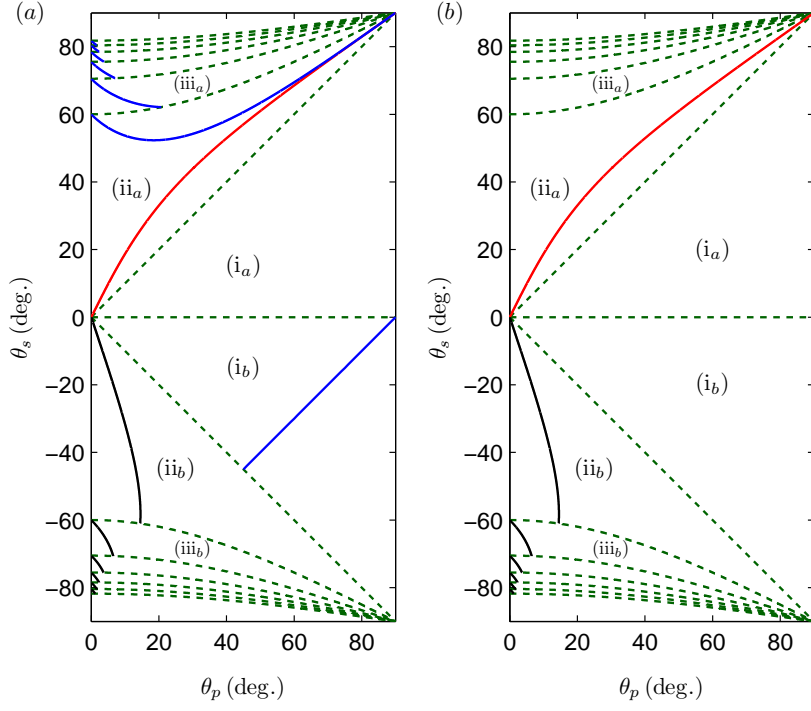
Figure 7. Contour lines of (a) $\hat{\varphi}_a^{(inv)} = 0$ and (b) $\hat{\varphi}_b^{(inv)} = 0$ in the (θ_p, θ_s) plane plotted as solid curves. Border lines for various $2 + N$ mode interactions, shown in Figure 5, are replotted for $1 \leq N \leq 7$ as green dotted curves. Red curves are identical to the $\theta_{d2} = 0$ contour line in Figure 6(b). The straight blue line in region (i_b) in (a) satisfies the condition (F.1) in Lee (2012).

Thus, red and black solid curves are identical in both Figures 7(a, b). Blue solid curves depict the conditions when $\hat{\varphi}_a^{(inv)} = 0$ but $\hat{\varphi}_b^{(inv)} \neq 0$.

If $\hat{\varphi}_b^{(inv)} = 0$ and, thus, $\hat{\varphi}_a^{(inv)} = 0$, the amplitude $A_{d(N-1)}$ grows exponentially as given by the first equation in (115), but A_{dN} becomes trivial. If $\hat{\varphi}_a^{(inv)} = 0$ but $\hat{\varphi}_b^{(inv)} \neq 0$, both $A_{d(N-1)}$ and A_{dN} grow exponentially as determined by (115). On the straight line in region (i_b) in Figure 7(a), both secondary and difference modes of a $2 + 1$ mode interaction grow exponentially as shown in Appendix F.1 in Lee (2012).

NUMERICAL RESULTS

All numerical results are obtained by using the logarithmic profile (7) and the parameter values listed in (14) and

$$\sigma = 0.0012. \tag{134}$$

The quantities are non-dimensionalized by U_a and Δ_a given in (8). With (4) and (14), the Charnock's (1955) constant becomes $\alpha_{CH} \equiv gz_o/u_*^2 = G/9.025 = 5.54 \times 10^{-3}$. The parameter values are chosen to show the characteristic behaviors of the solutions of amplitude equations.

Once the wave propagation angles of the primary and secondary wind waves, θ_p and θ_s, are selected, the wavenumbers, frequencies and other propagation angles are determined by (11)–(13), (30) and (32)–(34). The number of difference modes generated by a $2 + N$ mode interaction is determined by (15). The viscous parameter λ, defined by (66) and (80), is treated as a free parameter. The linear shape functions $\Phi_p^{(a)}$, $\Phi_s^{(a)}$ and $\Phi_{dn}^{(a)}$ are obtained by numerically solving (44). This solution is used to evaluate R_i, b_i and J_i by (51), (55) and (56). All parameters appearing in the amplitude equations are now determined.

The amplitude equations are solved subject to initial conditions. As mentioned before, only initial amplitudes of wind waves can be arbitrarily chosen. Those of the primary and secondary wind waves are chosen as

$$a_p = 1, \quad a_s = 0.001, \tag{135}$$

for all numerical results in this section. The initial amplitudes of all difference modes in a $2 + N$ mode interaction are determined by (98), (107) or (117) for the finite-viscosity, inviscid or viscous-limit case, respectively, if $N \geq 2$.

When $N \geq 2$, the primary and secondary wind waves remain linear as in (89). The first $N - 2$ difference-mode amplitudes, that also grow exponentially, are determined by (96), (106) and (116). The series solutions given in (122) are used to compute the amplitudes of the $(N-1)$th and Nth difference modes in the finite-viscosity and inviscid cases. For the results presented in this section, summations of less than 150 terms were sufficient to obtain convergent solutions. The integral equations (101), (102), (109) and (110) can also be numerically solved by using the procedure developed in Goldstein & Lee (1992) and Lee (1997, 2012). In the viscous limit, the last two difference-mode amplitudes are computed from the closed-form solutions (119).

Figure 8 illustrates the evolution of amplitudes in an inviscid $2 + 2$ mode interaction. The propagation angles of the primary and secondary wind waves are chosen to be $\theta_p = 30°$ and $\theta_s = -57°$ as denoted by the letters P and S in Figures 2(e, f). The nonlinear interaction generates two difference modes, denoted by D_1 and D_2, whose propagation angles are $\theta_{d1} \approx -79°$ and $\theta_{d2} \approx 83.5°$. The wave system in Figure 1(b) corresponds to this case.

The linear primary and secondary amplitudes, A_p and A_s, are shown in Figure 8(a). The amplitudes A_{d1} and A_{d2} of the first and second difference modes, computed using the finite-viscosity series solutions (122), are plotted in Figure 8(b) as solid curves. The initial exponential solutions (115), which are equal to the first terms in the series solutions, are shown as dot-dashed curves. The asymptotic solutions (129) and (130) are plotted as dotted curves. The amplitudes A_{d1} and A_{d2} grow exponentially in the linear stage where $\bar{t} < 0.5$ although they are nonlinearly generated. Both difference modes grow faster than the primary and secondary wind waves, and A_{d2} grows faster than A_{d1} in the initial linear stage. Once the primary amplitude reaches a certain level, say, at $\bar{t} \approx 0.5$, it starts to affect the growth of difference modes. In the later part of the parametric-growth stage where $\bar{t} > 2.5$, A_{d1} and A_{d2} grow

Figure 8. Inviscid $2 + 2$ mode critical-layer interaction when $\theta_p = 30°$, $\theta_s = -57°$ and $\lambda = 0$. (a) $\ln|A_p|$ (black), $\ln|A_s|$ (green); (b) $\ln|A_{d1}|$ (blue), $\ln|A_{d2}|$ (red); (c) $\mathrm{Re}(A'_{d1}/A_{d1})$ (blue), $\mathrm{Re}(A'_{d2}/A_{d2})$ (red); (d) $\mathrm{Im}(A'_{d1}/A_{d1})$ (blue), $\mathrm{Im}(A'_{d2}/A_{d2})$ (red) versus $\bar{t}$. Solid curves, $O(1)$-viscosity solutions; dot-dashed curves, initial exponentially-growing solutions; dotted curves, asymptotic solutions. Blue and red dotted curves are indistinguishable and only red dotted curves are visible in (c, d).

almost identically. They also grow faster than exponentially. In fact, they grow like the exponential-of-an-exponential as solid curves of the finite-viscosity solutions are indistinguishable from dotted curves of the asymptotic solutions in Figure 8(b). Transition from the initial exponential-growth stage to the later exponential-of-an-exponential-growth stage is shown to be gradual.

The real and imaginary parts of A'_{dn}/A_{dn}, plotted in Figures 8(c, d), represent the growth rate and wavelength reduction, respectively. The real part also represents the energy transfer rate since $(d|A_{dn}|^2/d\bar{t})/|A_{dn}|^2 = 2\text{Re}(A'_{dn}/A_{dn})$. The $O(1)$-viscosity solutions are shown as solid curves and the asymptotic solutions are plotted as dotted curves. In the figures, blue dotted curves for the 1st-difference mode are not distinguishable from red dotted ones for the 2nd-difference mode. The former is invisible since it is completely covered by the latter. In the initial exponential-growth stage, the 1st and 2nd difference modes have constant $\text{Re}(A'_{dn}/A_{dn})$ values of 2.64 and 3.64. In the entire stage, $\text{Re}(A'_{d1}/A_{d1} - \kappa_{d1})$ and $\text{Re}(A'_{d2}/A_{d2} - \kappa_{d2})$ are positive. As a result, $|A_{d1}|$ and $|A_{d2}|$ grow monotonically. The constant values of 1 and 1.64 for $\text{Re}(A'_p/A_p)$ and $\text{Re}(A'_s/A_s)$ are not plotted in the figure.

Results of the inviscid $2 + 2$ mode interaction when $\theta_p = 30°$ and $\theta_s = 50°$ are shown in Figure 9. The difference-mode propagation angles become $\theta_{d1} \approx 71.3°$ and $\theta_{d2} \approx -34.6°$. Four modes involved in this interaction are denoted by P, $\bar{S}$, $\bar{D}_1$ and $\bar{D}_2$ in Figures 2(e, f). The nonlinear growth effects start to become large near $\bar{t} \approx 2$. In the initial linear stage where A_{d1} and A_{d2} grow exponentially, the signs of $\text{Re}(A'_{d1}/A_{d1} - \kappa_{d1})$ and $\text{Re}(A'_{d2}/A_{d2} - \kappa_{d2})$ remain unchanged. Since they are negative in this case, the initial nonlinear effects tend to reduce the growth rates as one may observe in Figure 9(c). However, the continuing nonlinear effect enables the reverse of their signs for the eventual exponential-of-an-exponential growth of amplitudes. The finite-viscosity solutions shown as solid curves are not distinguishable from the asymptotic solutions plotted as dotted curves when $\bar{t} > 5$.

Effects of the viscous parameter λ on the growth of the first and second difference modes are shown in Figures 10(a, b) for the same values of $\theta_p = 30°$ and $\theta_s = -57°$ as in the inviscid case given in Figure 8. The value of λ is varied from 0 (inviscid) to 10^5. The finite-viscosity solutions are plotted as solid curves along with the corresponding viscous-limit solutions (119) as dashed curves. The asymptotic solutions computed by (129) and (130) are plotted as dotted curves. The linear primary and secondary wave amplitudes, shown in Figure 8(a), are not affected by λ. The finite-viscosity solutions when $\lambda = 10$ plotted as red curves are almost identical to the inviscid ones plotted as black curves in Figures 10(a, b). It is shown that the onset of the nonlinear growth is delayed as λ is increased, this can be identified as the departing point from the initial straight lines (not plotted here, but similar to the dot-dashed lines, for example, in Figure 8(b)). We also note that A_{d1} and A_{d2} grow almost identically in the nonlinear growth stage for all λ values considered. The inviscid and all finite-viscosity solutions approach the exponential-of-an-exponential asymptotic solutions as $\bar{t} \to \infty$. Even for large values of λ, the evolution of A_{d1} and A_{d2} in later nonlinear growth stage is approximately described by the asymptotic solutions plotted as dotted curves. It is worth pointing out that there is no arbitrary parameter in the asymptotic solutions (129) and (130).

As λ becomes large, the $O(1)$-viscosity solution plotted as solid curves in Figure 10 approaches the viscous-limit solution plotted as dashed curves, especially, in the initial stage. This mainly occurs because the initial amplitude a_{dn} of the $O(1)$-viscosity solution approaches $a_{dn}^{(vlim)}$ of the viscous-limit solution. The growth rates are independent of λ in the initial linear stage. When $\lambda = 10^5$, the finite-viscosity solution closely follows the viscous-limit solution during the initial linear stage and, also, in the beginning portion of nonlinear stage, then it jumps onto the asymptotic solution rather abruptly. Although they are plotted for different values of λ, in order to compare against the corresponding finite-viscosity solutions, λ is not an independent parameter for the viscous-limit solutions.
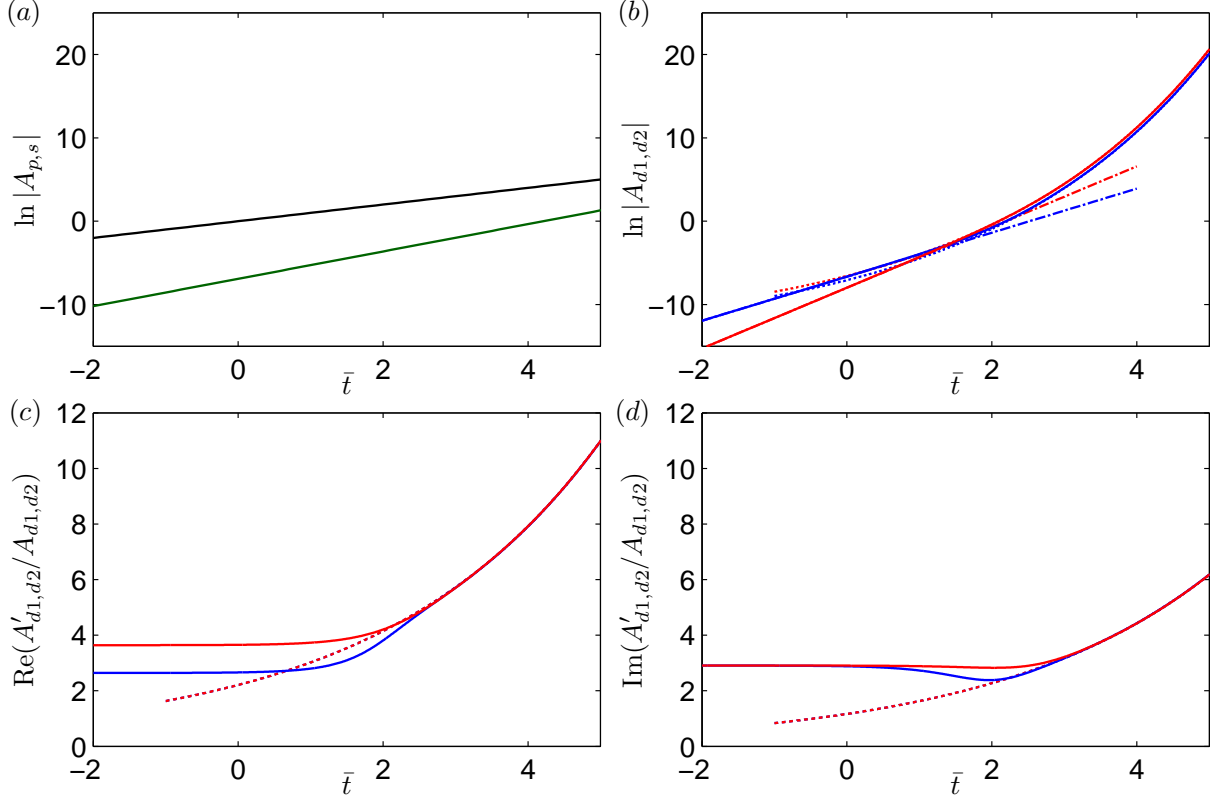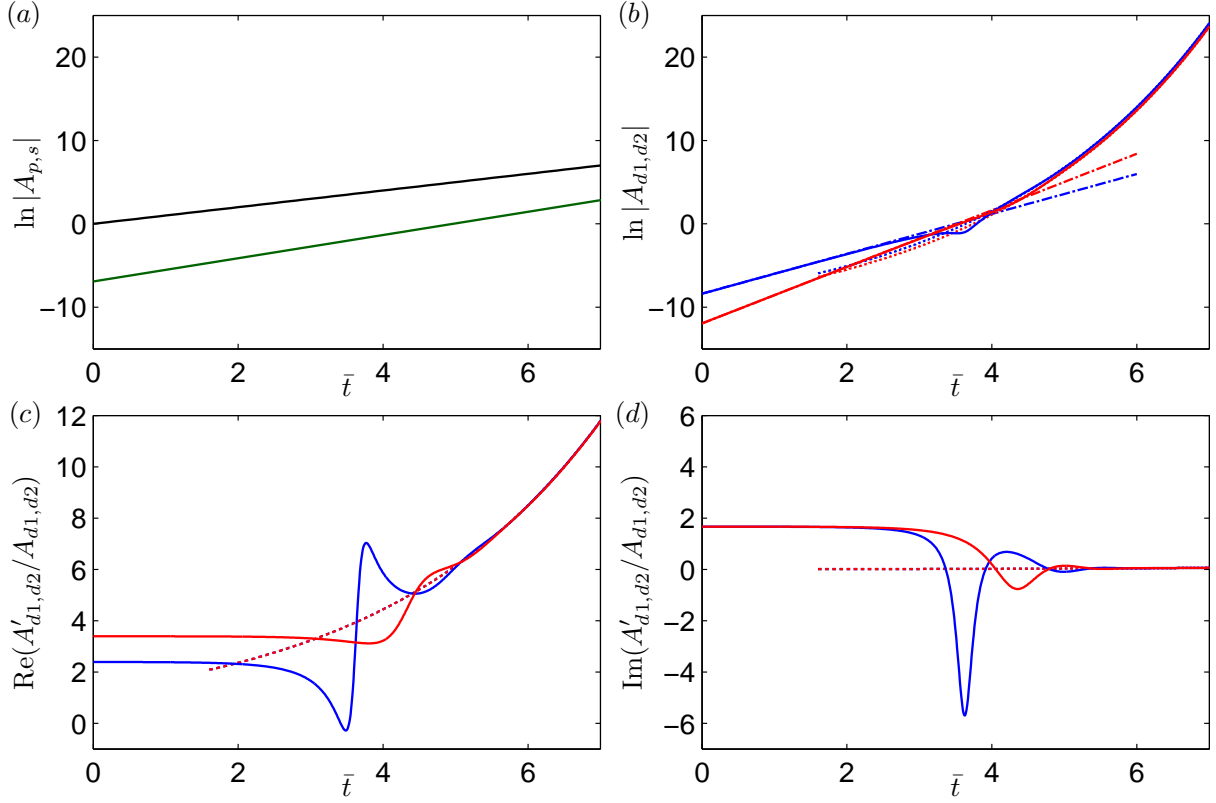
Figure 9. Inviscid $2+2$ mode critical-layer interaction when $\theta_p = 30°$, $\theta_s = 50°$ and $\lambda = 0$. (a) $\ln|A_p|$ (black), $\ln|A_s|$ (green); (b) $\ln|A_{d1}|$ (blue), $\ln|A_{d2}|$ (red); (c) $\operatorname{Re}(A'_{d1}/A_{d1})$ (blue), $\operatorname{Re}(A'_{d2}/A_{d2})$ (red); (d) $\operatorname{Im}(A'_{d1}/A_{d1})$ (blue), $\operatorname{Im}(A'_{d2}/A_{d2})$ (red) versus $\bar{t}$. Solid curves, $O(1)$-viscosity solutions; dot-dashed curves, initial exponentially-growing solutions; dotted curves, asymptotic solutions. Blue and red dotted curves are indistinguishable and only red dotted curves are visible in (c, d).
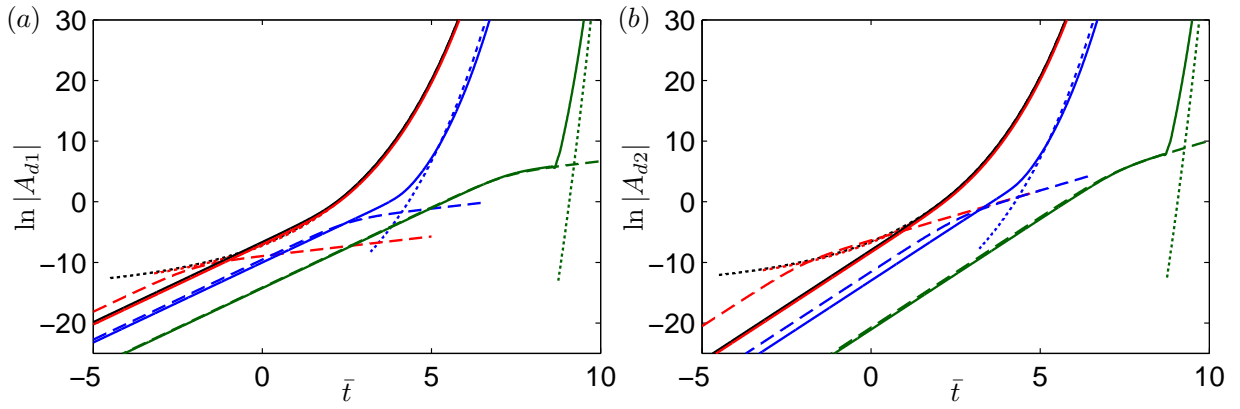
Figure 10. Effect of viscosity on a $2+2$ mode interaction when $\theta_p = 30°$ and $\theta_s = -57°$. $\lambda = 0$ (inviscid, black), 10 (red), 10^3 (blue) and 10^5 (green). (a) $\ln|A_{d1}|$ and (b) $\ln|A_{d2}|$ versus $\bar{t}$. Solid curves, $O(1)$-viscosity solutions; dashed curves, viscous-limit solutions; dotted curves, asymptotic solutions.

33
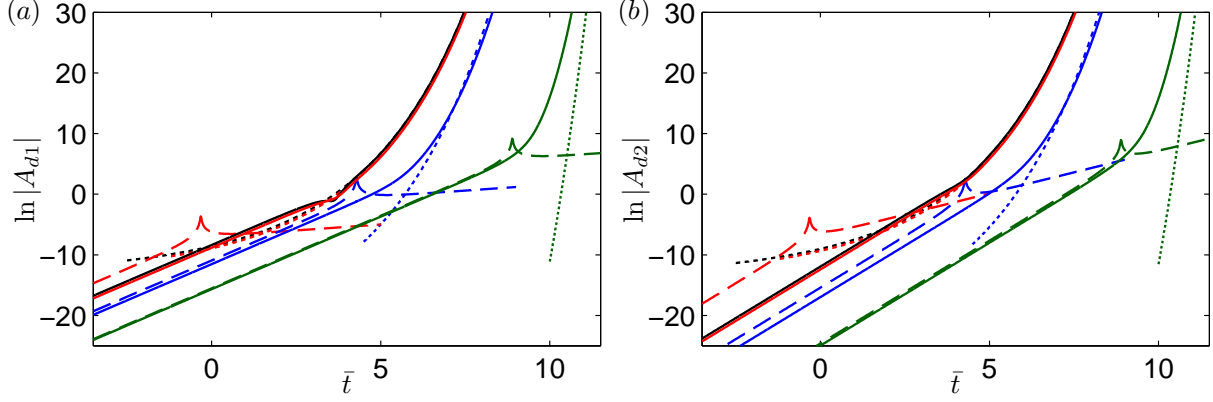
Figure 11. Effect of viscosity on a $2+2$ mode interaction when $\theta_p = 30°$ and $\theta_s = 50°$. $\lambda = 0$ (inviscid, black), 10 (red), 10^3 (blue) and 10^5 (green). (a) $\ln|A_{d1}|$ and (b) $\ln|A_{d2}|$ versus $\bar{t}$. Solid curves, $O(1)$-viscosity solutions; dashed curves, viscous-limit solutions; dotted curves, asymptotic solutions.

Figure 11 shows that large viscosity also delays the onset of the nonlinear growth when $\theta_p = 30°$ and $\theta_s = 50°$. The primary and secondary amplitudes are the same as those plotted in Figure 9(a). Note that there are spikes in the viscous-limit solutions plotted as dashed curves in Figure 11. They are due to near singular behavior of the viscous-limit solutions (119). The viscous-limit solution can actually become singular for certain combinations of θ_p and θ_s.

Numerical results of an inviscid $2+3$ mode interaction are plotted in Figure 12. When $\theta_p = 30°$ and $\theta_s = -70°$, the $2+3$ mode interaction generates three difference modes with propagation angles of $(\theta_{d1}, \theta_{d2}, \theta_{d3}) \approx (-78.5°, -86.2°, 86.9°)$. The primary, secondary and difference modes denoted by P, S, D_1, D_2 and D_3 in Figures 2(g, h) correspond to this specific case. As plotted in Figure 12(a), the first-difference mode, in addition to the primary and secondary waves, grows exponentially. The last two difference-mode amplitudes, A_{d2} and A_{d3} plotted as solid curves in Figure 12(b), grow faster than exponentially.

The viscous effects on the above $2+3$ mode interaction are shown in Figure 13. The linear primary and secondary wave amplitudes, which are independent of λ, are given in Figure 12(a). Although the growth rate of the exponentially-growing first-difference mode is not affected by the viscosity as shown by (97), its initial amplitude determined by (98) is a function of λ. The complex a_{d1} becomes $(-1.7 - 1.3\mathrm{i}) \times 10^{-3}$, $(0.2 - 2.2\mathrm{i}) \times 10^{-3}$, $(9.4 + 0.1\mathrm{i}) \times 10^{-5}$ and $(1.1 + 0.5\mathrm{i}) \times 10^{-6}$, when $\lambda = 0$, 10, 10^3 and 10^5, respectively. Effects of λ on the growth of the 2nd and 3rd difference modes are shown in Figure 13.

Figure 14 shows the numerical results of the inviscid $2+4$ mode interaction when $\theta_p = 30°$ and $\theta_s = -76°$. The $2+4$ mode interaction generates four difference modes with propagation angles of $(\theta_{d1}, \theta_{d2}, \theta_{d3}, \theta_{d4}) \approx (-80.2°, -84.2°, -87.9°, 88.6°)$. The linear primary (black) and secondary (green) waves and the first (purple) and second (brown) difference modes are shown in Figure 14(a). Their growth rates are $\kappa_p(= 1)$, $\kappa_s(\approx 2.87 - 13.71\mathrm{i})$, $\kappa_{d1} = \kappa_s^* + \kappa_p$ and $\kappa_{d2} = \kappa_{d1} + \kappa_p$. Also, the initial growth rates of the third (blue) and fourth (red) difference modes become $\kappa_{d3} = \kappa_{d2} + \kappa_p$ and $\kappa_{d4} = \kappa_{d3} + \kappa_p$ as shown in Figure 14(b). The amplitudes A_{d3} and A_{d4} are first reduced at the beginning of the nonlinear growth stage, but they soon approach the asymptotic solutions plotted as dotted curves. Figure 15 shows the evolution of A_{d3} and A_{d4} for various values of λ.

Effects of secondary-wave propagation angles on $2+N$ mode interactions are investigated by vary-
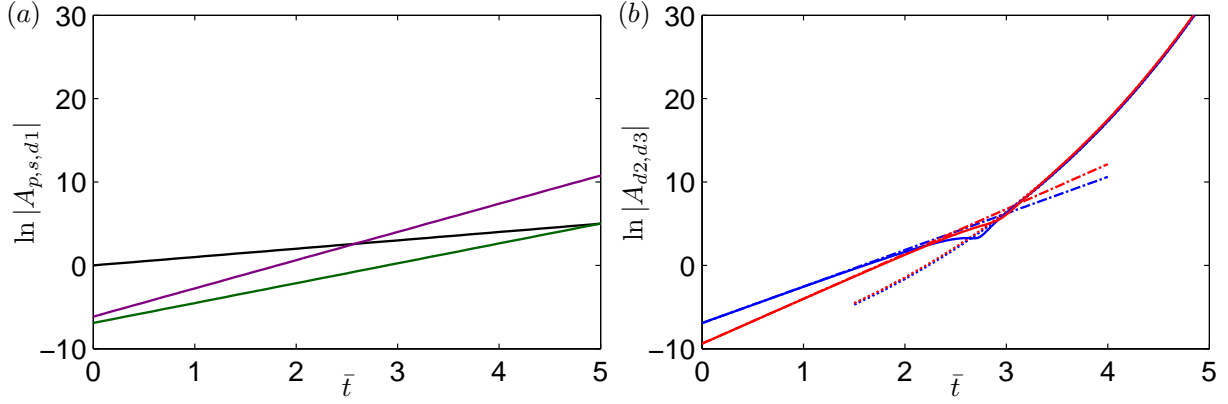
Figure 12. Inviscid 2+3 mode critical-layer interaction when $\theta_p = 30°$, $\theta_s = -70°$ and $\lambda = 0$. (a) $\ln|A_p|$ (black), $\ln|A_s|$ (green), $\ln|A_{d1}|$ (purple); (b) $\ln|A_{d2}|$ (blue), $\ln|A_{d3}|$ (red) versus $\bar{t}$. Solid curves, $O(1)$-viscosity solutions; dot-dashed curves, initial exponentially-growing solutions; dotted curves, asymptotic solutions.
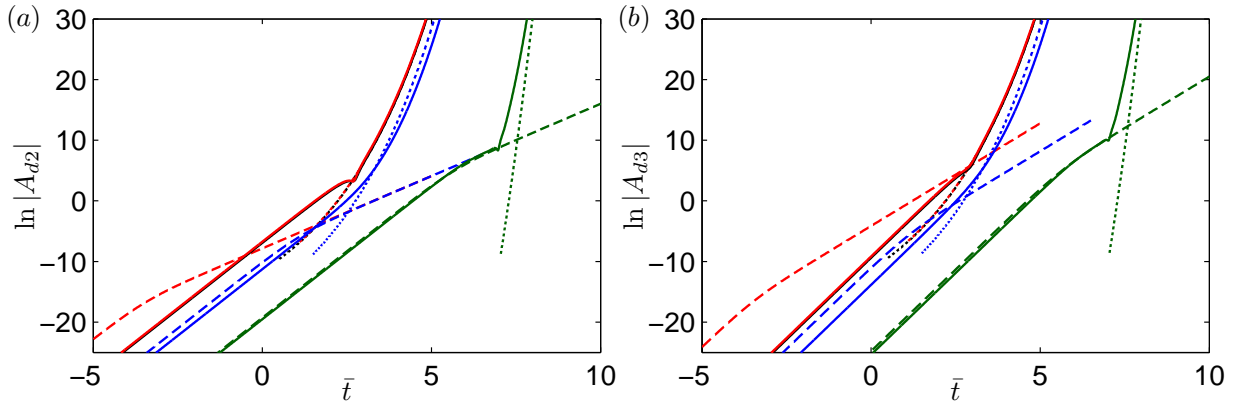
Figure 13. Effect of viscosity on a 2+3 mode interaction when $\theta_p = 30°$ and $\theta_s = -70°$. $\lambda = 0$ (inviscid, black), 10 (red), 10^3 (blue) and 10^5 (green). (a) $\ln|A_{d2}|$ and (b) $\ln|A_{d3}|$ versus $\bar{t}$. Solid curves, $O(1)$-viscosity solutions; dashed curves, viscous-limit solutions; dotted curves, asymptotic solutions.
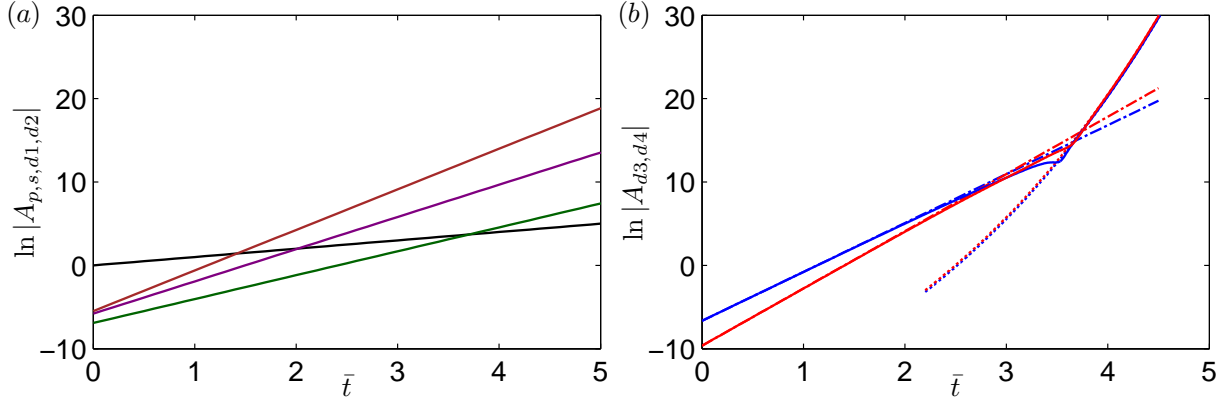
Figure 14. Inviscid 2+4 mode critical-layer interaction when $\theta_p = 30°$, $\theta_s = -76°$ and $\lambda = 0$. (a) $\ln|A_p|$ (black), $\ln|A_s|$ (green), $\ln|A_{d1}|$ (purple), $\ln|A_{d2}|$ (brown); (b) $\ln|A_{d3}|$ (blue), $\ln|A_{d4}|$ (red) versus $\bar{t}$. Solid curves, $O(1)$-viscosity solutions; dot-dashed curves, initial exponentially-growing solutions; dotted curves, asymptotic solutions.
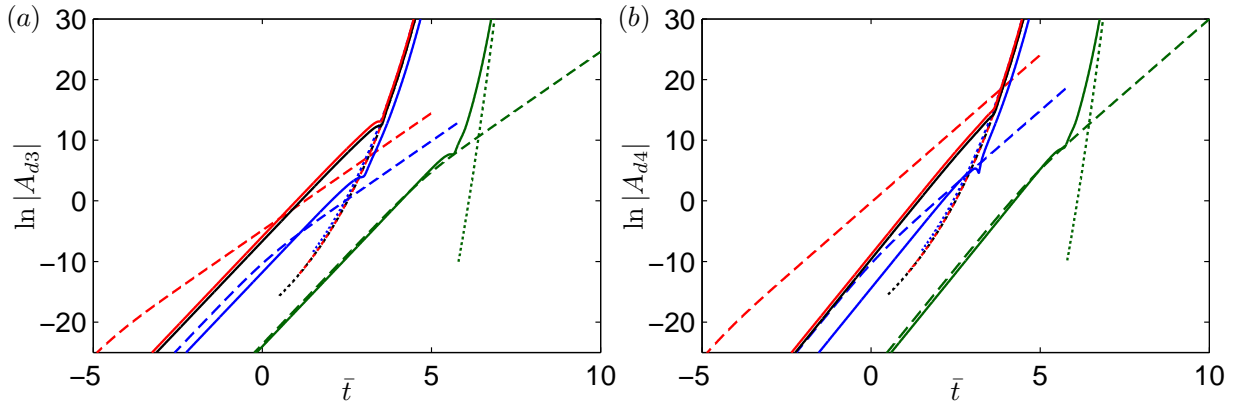
Figure 15. Effect of viscosity on a 2+4 mode interaction when $\theta_p = 30°$ and $\theta_s = -76°$. $\lambda = 0$ (inviscid, black), 10 (red), 10^3 (blue) and 10^5 (green). (a) $\ln|A_{d3}|$ and (b) $\ln|A_{d4}|$ versus $\bar{t}$. Solid curves, $O(1)$-viscosity solutions; dashed curves, viscous-limit solutions; dotted curves, asymptotic solutions.

ing θ_s while keeping θ_p unchanged. The value of θ_s is varied from $-89°$ to $89°$ with increments of $0.05°$ for the inviscid and $0.1°$ for the viscous case. The series solutions are numerically evaluated for each set of (θ_p, θ_s) combinations. The results from various sets of (θ_p, θ_s) combinations are then assembled to obtain the amplitudes as functions of θ_s at given values of $\bar{t}$. Figure 16 shows the results of this parameter study when $\theta_p = 30°$. The absolute values of the amplitudes, $|A_\imath|$, where $\imath = \{p, s, d1, d2, d3\}$ for the primary, secondary, 1st-difference, 2nd-difference and 3rd-difference modes, are plotted in the first/leftmost to fifth/rightmost columns of sub-figures. The effects of viscosity are also investigated by varying $\lambda = 0$ (inviscid, 1st/top row), 10 (2nd row), 10^3 (3rd row) and 10^5 (4th/bottom row). In the figures, $|A_\imath|$ versus θ_s are plotted at $\bar{t} = 0$, 3, 6, 9 and 12 (only when $\lambda = 10^5$). The wave propagation angles of difference modes, θ_{d1}, θ_{d2} and θ_{d3}, as functions of θ_s for a constant $\theta_p = 30°$ can be found from Figure 6. For the fixed value of $\theta_p = 30°$, the amplitude of the linear primary wave, A_p, is independent of θ_s and λ as shown in the first column of sub-figures in Figure 16.

The $2 + 1$ mode interaction occurs when $0 < |\theta_s| < 30°$ as one can find from Figure 5. The cyan-color-filled sections in the color bar plotted on top of each sub-figures in Figure 16 correspond to these ranges of θ_s. The $2 + 1$ mode interaction produces nonlinear growth effects on the secondary and (1st) difference mode amplitudes, A_s and $A_{d1}(\equiv A_d)$, as shown in the 2nd and 3rd columns of sub-figures. Since the $2 + 1$ mode interaction only generates a single (1st) difference mode, the corresponding regions to the cyan-color-filled sections in the 4th and 5th columns of sub-figures, i.e. for the 2nd and 3rd difference modes, are empty. Differences between the results of the inviscid $2 + 1$ mode interactions in Figures 16 (b, c) and those plotted in Figures 10(a, b) in Lee (2012) are due to different normalizations of variables. The nonlinear effect is stronger when θ_s is negative than when it is positive. The effect of viscosity is shown to delay the onset of the nonlinear growth. The value of θ_s for the largest $|A_s|$ and $|A_{d1}|$ at $\bar{t} = 9$ becomes closer to $-\theta_p$ as the viscous effect is increased. Details of amplitude evolution when $(\theta_p, \theta_s) = (30°, -15°)$ can be found in Figures 6 and 8 in Lee (2012).

If $30° < |\theta_s| < 64.34°$, that corresponds to the yellow-color-filled sections in the color bars, the $2 + 2$ mode interactions occur. The secondary wave remains linear as shown in the 2nd column of sub-figures. Its linear growth rate that is independent of λ, can be found in Figure 1 in Lee (2012). The amplitudes of the first and second difference modes are nonlinearly affected. The amplitudes $|A_{d1}|$ and $|A_{d2}|$ grow faster for negative values of θ_s compared to the positive ones as in $2 + 1$ mode interactions. The value of $\theta_s = -57°$ for the detailed study presented in Figures 8 and 10 was chosen to show the results near the strongest $2 + 2$ mode interaction when $\theta_p = 30°$.

The $2 + 3$ mode interaction occurs when $64.34° < |\theta_s| < 73.22°$, or in the orange-color-filled sections in the color bars in Figure 16. Both secondary and first-difference modes grow exponentially as shown in the 2nd and 3rd columns of sub-figures. The amplitudes of the second and third difference modes, plotted in the 4th and 5th columns, are nonlinearly affected.

If $73.22° < |\theta_s| < 77.5°$, as in the black-color-filled sections, the $2 + 4$ mode interaction occurs. The amplitudes A_s, A_{d1} and A_{d2} grow exponentially. The nonlinearly-growing A_{d3} is plotted in the rightmost column of sub-figures. The fourth-difference mode amplitude, A_{d4}, is not shown in the figure.

There are special combinations of (θ_p, θ_s) for which the nonlinear effects are reduced or disappear. When $\theta_s = 0$, the linear plane secondary wave, that propagates along the downwind direction, grows exponentially. The difference mode is not generated by the nonlinear interaction of the oblique primary and plane secondary waves. If $\theta_s = -\theta_p$, the linear secondary mode grows exponentially as shown in Figure 16. The difference mode becomes steady and spanwise periodic. When $\theta_s = \theta_p$, the nonlinear interaction of the primary oblique wave interacting with itself does not generate a difference mode (Goldstein & Leib 1989). If θ_s equals the plus/minus wave propagation angle corresponding to $\alpha_s = N\alpha_p$ for $N \geq 2$, the first $N - 1$ difference modes grow exponentially as confirmed in Figure 16. The

Nth-difference mode becomes steady and spanwise periodic.

It is found that a $2+2$ mode interaction can generate a plane 2nd-difference mode when the relation (131) is satisfied. With the parameter values in (14), the pair of $(\theta_p, \theta_s) \approx (30°, 43.87°)$ satisfies the condition independently of λ.

In Figure 7, we find that both coefficients $\hat{\varphi}_a^{(inv)}$ and $\hat{\varphi}_b^{(inv)}$ in the inviscid amplitude equations (109) and (110) vanish when the 2nd-difference mode is a plane wave, the case already considered above. Figure 7 also shows that $\hat{\varphi}_a^{(inv)} = 0$ but $\hat{\varphi}_b^{(inv)} \neq 0$, for example, if (θ_p, θ_s) equals $(30°, 54.21°)$ for a $2+2$ mode interaction. The amplitudes A_{d1} and A_{d2} grow exponentially as shown in Figures 16(c, d). We also find from Figure 16 that this inviscid effect disappears as λ is increased.

In Figures 17 and 18, the results of a parameter study when $\theta_p = 50°$ and $70°$, respectively, are summarized. Effects of θ_s on various $2+N$ mode interactions are investigated by varying θ_s from $-89°$ to $89°$ as in the previous $\theta_p = 30°$ case. The regions of various $2+N$ mode interactions are shown as color-filled sections in the color bars. The values of $|\theta_s|$ at the boundaries where $\alpha_s = N\alpha_p$ become $50°$, $71.25°$, $77.63°$ and $80.75°$ if $\theta_p = 50°$ for $N = 1, 2, 3$ and 4 as can be found from Figure 5. They are $70°$, $80.15°$, $83.45°$ and $85.09°$ if $\theta_p = 70°$. Differences between the results of the inviscid $2+1$ mode interactions in Figures 18 (b, c) and those plotted in Figures 11(a, b) in Lee (2012) are due to different normalizations of variables. The results of these $\theta_p = 50°$ and $70°$ cases are consistent with those of the $\theta_p = 30°$ case. The nonlinear parametric growth is more effectively enhanced when the sign of the propagation angle of the secondary wind wave θ_s is opposite to that of the primary wind wave θ_p than when both have the same sign.

Figure 16. Effects of θ_s and λ on $2+N$ mode interactions when $\theta_p = 30°$. (a, f, k, p) $\ln |A_p|$, (b, g, l, q) $\ln |A_s|$, (c, h, m, r) $\ln |A_{d1}|$, (d, i, n, s) $\ln |A_{d2}|$, (e, j, o, t) $\ln |A_{d2}|$ versus θ_s. (a–e) $\lambda = 0$ (inviscid), (f–j) $\lambda = 10$, (k–o) $\lambda = 10^3$, (p–t) $\lambda = 10^5$. Solid curves depict A_t at various $\bar{t}$. Black curves, $\bar{t} = 0$; blue curves, $\bar{t} = 3$; green curves, $\bar{t} = 6$; red curves, $\bar{t} = 9$; purple curves, $\bar{t} = 12$ (only when $\lambda = 10^5$). Color-filled-sections in the color bar on top of each sub-figures represent various $2+N$ mode interactions. Cyan-color-filled, $N = 1$; yellow-color-filled, $N = 2$; orange-color-filled, $N = 3$; black-color-filled, $N = 4$.

39
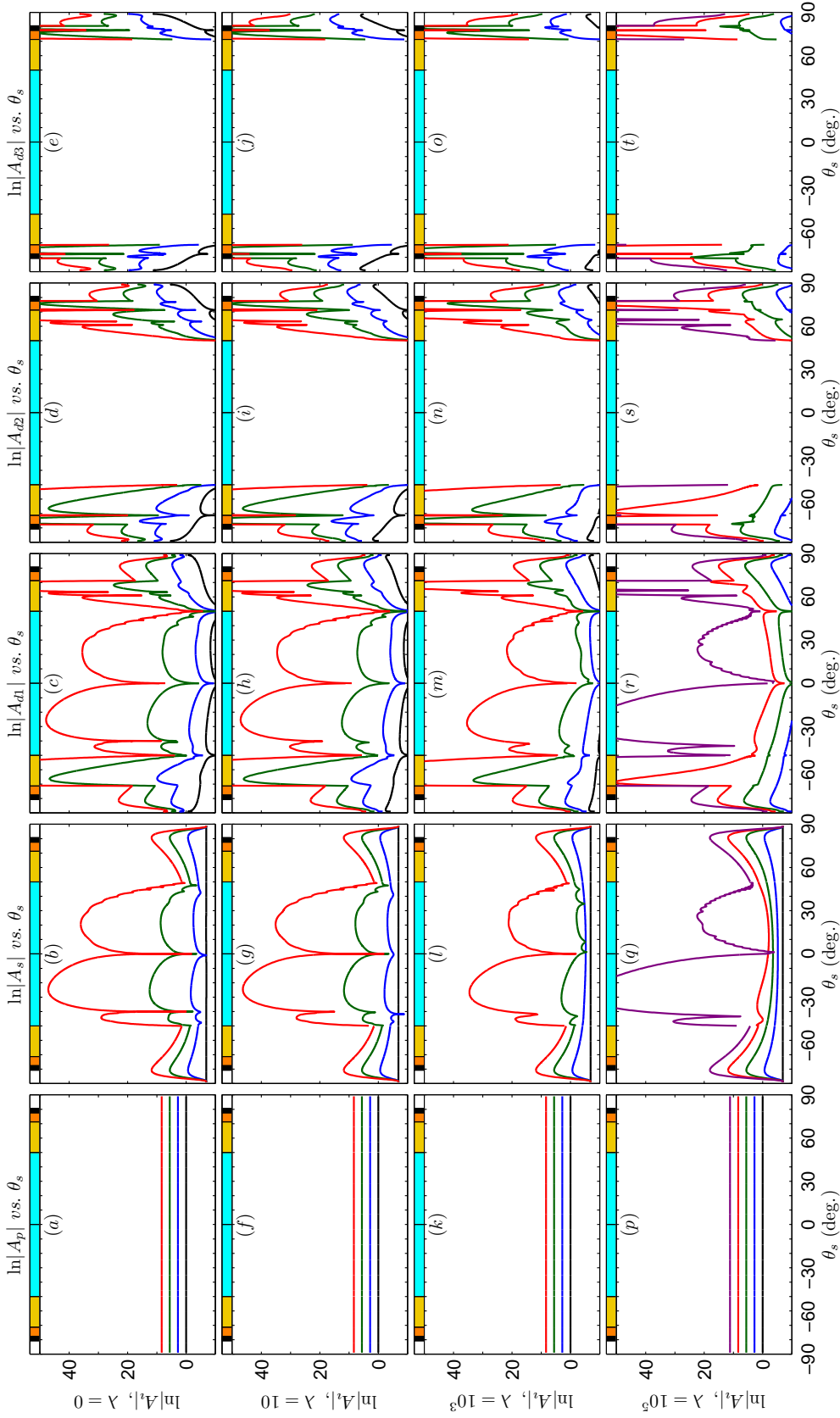
Figure 17. Effects of θ_s and λ on $2 + N$ mode interactions when $\theta_p = 50°$. (a, f, k, p) $\ln|A_p|$, (b, g, l, q) $\ln|A_s|$, (c, h, m, r) $\ln|A_{d1}|$, (d, i, n, s) $\ln|A_{d2}|$, (e, j, o, t) $\ln|A_{d3}|$ versus θ_s. (a–e) $\lambda = 0$ (inviscid), (f–j) $\lambda = 10$, (k–o) $\lambda = 10^3$, (p–t) $\lambda = 10^5$. Solid curves depict A_t at various $\bar{t}$. Black curves, $\bar{t} = 0$; blue curves, $\bar{t} = 1$; green curves, $\bar{t} = 2$; red curves, $\bar{t} = 3$; purple curves, $\bar{t} = 4$ (only when $\lambda = 10^5$). Color-filled-sections in the color bar on top of each sub-figures represent various $2 + N$ mode interactions. Cyan-color-filled, $N = 1$; yellow-color-filled, $N = 2$; orange-color-filled, $N = 3$; black-color-filled, $N = 4$.
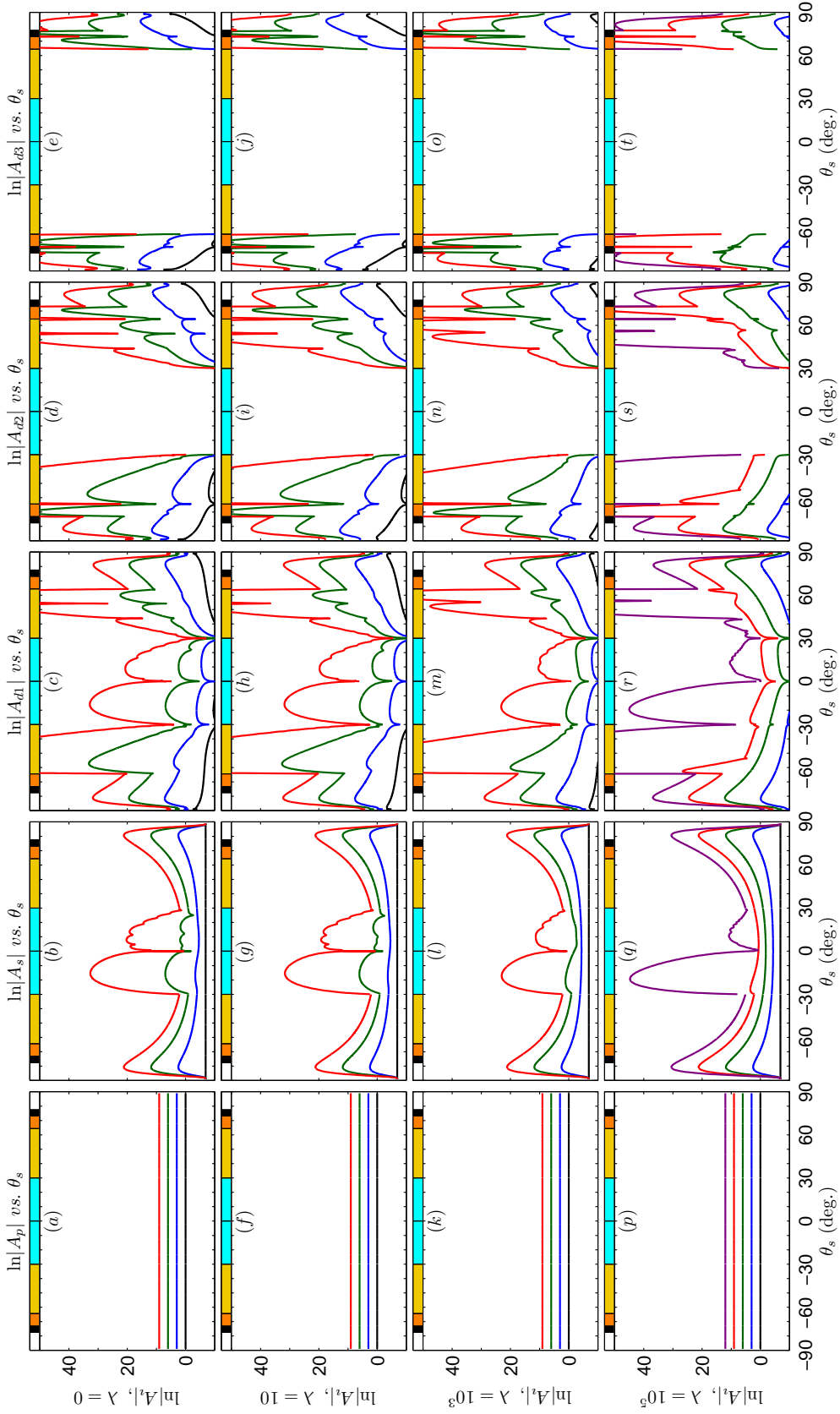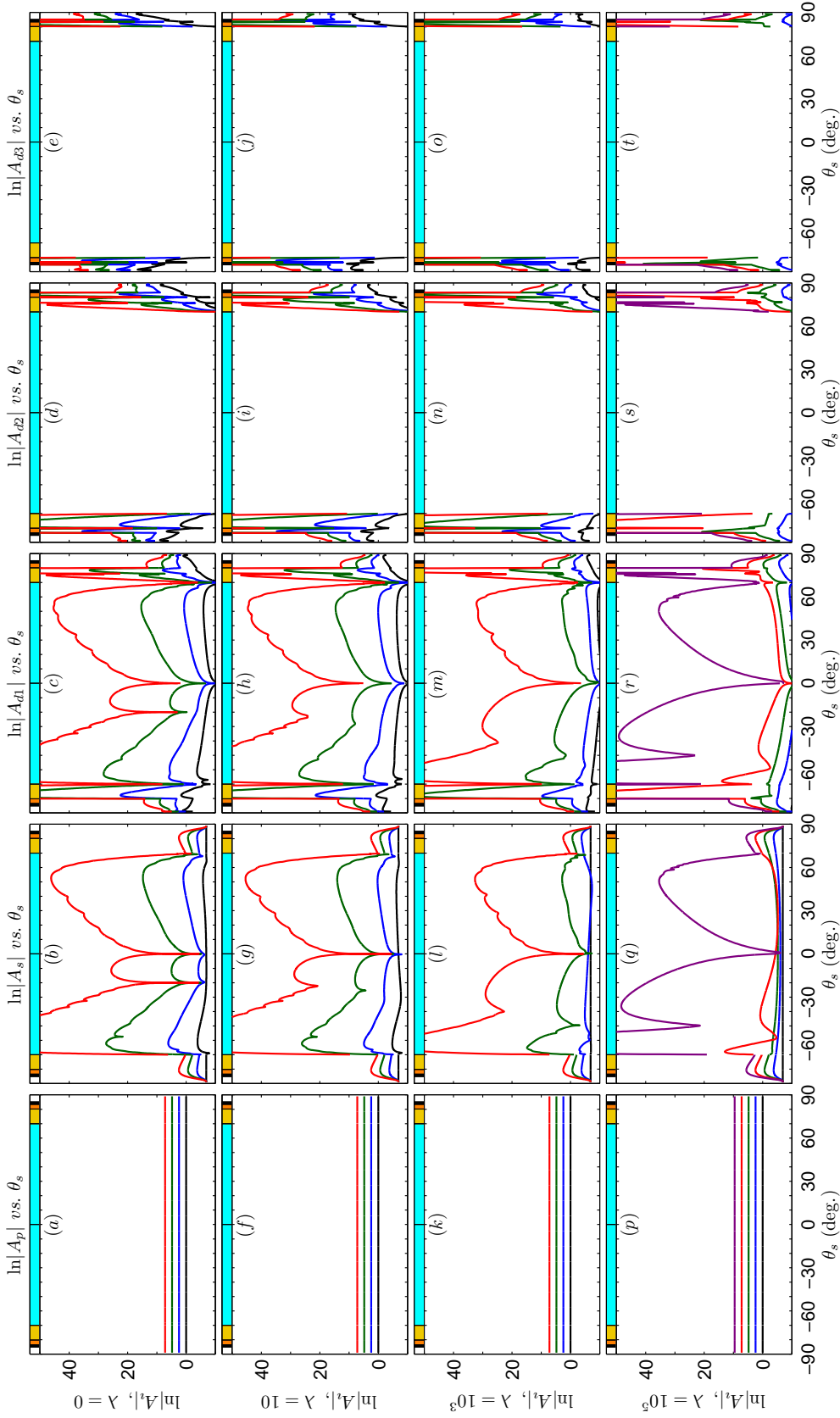
Figure 18. Effects of θ_s and λ on $2+N$ mode interactions when $\theta_p = 70°$. (a, f, k, p) $\ln|A_p|$, (b, g, l, q) $\ln|A_s|$, (c, h, m, r) $\ln|A_{d1}|$, (d, i, n, s) $\ln|A_{d2}|$, (e, j, o, t) $\ln|A_{d3}|$ versus θ_s. (a–e) $\lambda = 0$ (inviscid), (f–j) $\lambda = 10$, (k–o) $\lambda = 10^3$, (p–t) $\lambda = 10^5$. Solid curves depict A_t at various $\bar{t}$. Black curves, $\bar{t} = 0$; blue curves, $\bar{t} = 1$; green curves, $\bar{t} = 2$; red curves, $\bar{t} = 3$; purple curves, $\bar{t} = 4$ (only when $\lambda = 10^5$). Color-filled-sections in the color bar on top of each sub-figures represent various $2+N$ mode interactions. Cyan-color-filled, $N = 1$; yellow-color-filled, $N = 2$; orange-color-filled, $N = 3$; black-color-filled, $N = 4$.

41

DISCUSSION AND CONCLUSIONS

A nonlinear interaction that can generate low-frequency fluctuations in the air above obliquely propagating wind waves is studied. The nonlinear interaction can be initiated by two three-dimensional fluctuations in wind, which are induced by wind-driven surface waves, referred to as the primary and secondary waves. The secondary-wave frequency can be higher than the primary frequency. The analysis is valid for general two-dimensional wind profiles. The characteristic wave speed is assumed to be sufficiently large, so that the critical layer is distinct from the viscous sublayer. The experimental study by Hristov, Miller & Friehe (2003) has shown the existence of distinct critical layers in an open ocean.

As pointed out in Lee (2012), the phase speed in the wave propagation direction of an oblique wave, $\bar{c}_\iota$, becomes

$$\bar{c}_\iota \equiv \omega_\iota/\gamma_\iota = c \cos\theta_\iota, \tag{136}$$

for $\iota = \{p, s, d1, \ldots, dN\}$, where γ_ι, θ_ι and ω_ι are defined by (12), (13) and (32)–(34), and c is the wave speed in the streamwise or downwind direction (Drazin & Reid 2004, p. 128). For wind waves and nonlinear difference modes with an equal wave speed in downwind direction c, the phase speeds $\bar{c}_\iota$ are proportional to $\cos\theta_\iota$. For an equal phase speed $\bar{c}_\iota$, the wave speed in downwind direction c becomes larger and the critical level moves higher from the interface as the wave propagation angle is increased. An oblique wind wave may have a distinct critical layer from the viscous sublayer although its phase speed $\bar{c}_\iota$ is small.

We suppose that the primary wind wave is the largest oblique wave in an initial wind-driven wave field. The linear primary wave grows exponentially. According to Miles' (1957) theory, its growth rate is proportional to σ, that is the density ratio of air to water as in (1). The typical value of σ is $O(10^{-3})$. Once the steepness of the primary wind wave becomes $O(\sigma^3)$, it can nonlinearly interact with a secondary oblique wave of smaller steepness. If the wave speeds in downwind direction of the primary and secondary oblique waves are equal, both wind waves share a common critical layer where the nonlinear interaction first takes place (Davis 1969; Benney & Bergeron 1969; Drazin & Reid 2004). If N is the smallest integer not less than the ratio of the secondary to primary frequencies, or if the frequency ratio is greater than $N-1$ but less than N, as in (15) and (16), the critical-layer interaction generates N difference modes. The $2 + N$ mode interaction is composed of two wind waves and N nonlinearly generated difference modes. A plane surface wave, propagating in the streamwise direction, whose steepness is larger than the primary oblique wave can coexist without playing any significant role in the present nonlinear interaction stage.

When $N \geq 2$, the interaction between the primary and secondary wind waves generates the first-difference mode. The primary wave then couples with the first-difference mode to generate the second-difference mode. This sequential difference-mode-generation process is continued until the Nth-difference mode is generated by the quadratic interaction of the primary and $(N-1)$th-difference modes. The critical-layer interaction between the primary and Nth-difference modes produces a nonlinear effect on the $(N-1)$th-difference mode. The amplitudes of difference modes are of the same order of magnitude as the secondary-wave amplitude in air. Both primary and secondary wind waves remain linear. The first $N-2$ difference modes, whose frequencies are higher than the primary frequency as in (36), grow exponentially although they are nonlinearly generated. The growth rate of the nth-difference mode, or initial growth rate of the $(N-1)$th or Nth difference mode, is increased by $n\kappa_p$ from κ_s^* as shown in (97) for $1 \leq n \leq N$. Meanwhile, its frequency ω_{dn} is decreased by $n\omega_p$ from the highest ω_s as obtained from (34) for $1 \leq n \leq N-1$. The κ_p and κ_s are the linear growth rates of the primary

and secondary waves, and ω_p $(= \alpha_p c)$ and ω_s $(= \alpha_s c)$ are their frequencies. The amplitudes of the $(N-1)$th and Nth difference modes are governed by coupled integral equations, if they do not satisfy the free-surface-wave dispersion relation (11). Numerical results show that they can grow faster than exponentially. In fact, both of them can grow like the exponential-of-an-exponential in the inviscid and finite-viscosity cases. The frequencies of the last two difference modes are lower than the primary frequency as shown by (36). In the special case where the relation (11) is satisfied by a difference mode, the amplitude will be governed by an integro-differential equation that is similar to that of a secondary wave in Lee (2012).

The nonlinear growth in a $2 + N$ mode interaction is of the parametric-growth type. The coupling between the primary and Nth-difference modes produces a nonlinear effect on the $(N-1)$th-difference mode if $N \geq 2$. When $N = 1$, the quadratic interaction between the primary and difference modes produces a nonlinear growth of the secondary mode.

It is shown that the $2 + N$ mode critical-layer interaction greatly enhances the growth of oblique modes whose frequencies are lower than the primary frequency. They are the $(N-1)$th and Nth difference modes if $N \geq 2$, and the secondary wind wave and difference mode when $N = 1$. Due to nonlinear effects, the amplitudes of these modes can quickly become as large as the primary-wave amplitude, i.e. $O(\sigma^3)$. Their nonlinear coupling in a following stage can generate multiple difference modes whose amplitudes are $O(\sigma^3)$. The nonlinear interaction in this stage will still be of a quadratic-interaction type, by which any combination of two modes can interact to generate a difference mode or produce a nonlinear effect on it. The most amplified modes whose amplitudes first become $O(\sigma^{5/2})$ may then enter the next self-interaction stage. Lee & Wundrow (2011) show that these modes in the self-interaction stage can grow even faster than they do in the parametric-growth stages.

Although the $2 + N$ mode interaction is induced by wind-driven surface waves, the most rapidly growing mode in air may not be the one that is associated with a wind wave. For example, if $N \geq 2$, the $(N-1)$th and Nth difference modes, that can grow faster than exponentially, do not satisfy the free-surface-wave dispersion relation. The amplitudes of the corresponding disturbances in water are reduced by a factor of $O(\sigma)$ as shown in (28) and (42). For this interaction, there might be hardly any observable evidence of nonlinear effects on the water surface although the difference modes in air have already become as large as the primary wave. This indicates that the multi-mode-generation process in air may start earlier than in water.

The critical-layer interaction could play an important role in the growth of perturbations in the wind over water. One of the results of the present analysis is that the $2 + N$ mode critical-layer interaction, occurring in the air over wind-driven surface waves, can nonlinearly enhance the growth of air fluctuations whose frequencies are lower than the primary frequency.

This page intentionally left blank.

REFERENCES

ALEXAKIS, A., YOUNG, Y-N & ROSNER, R. 2004 Weakly nonlinear analysis of wind-driven gravity waves. *J. Fluid Mech.* **503**, 171-200.

BENNEY, D.J. & BERGERON, R.F, JR. 1969 A new class of nonlinear waves in parallel flows. *Stud. Appl. Math.* **48**, 181-204.

CHARNOCK, H. 1955 Wind stress on a water surface. *Q. J. R. Met. Soc.* **81**, 639-640.

DAVIS, R.E. 1969 On the high Reynolds number flow over a wavy boundary. *J. Fluid Mech.* **36**, 337-346.

DRAZIN, P.G. & REID W.H. 2004 *Hydrodynamic Stability,* 2nd edn. Cambridge University Press.

GOLDSTEIN, M.E. & CHOI, S.W. 1989 Nonlinear evolution of interacting oblique waves on two–dimensional shear layers. *J. Fluid Mech.* **207**, 97-120. Also Corrigendum, *J. Fluid Mech.* **216**, 659-663.

GOLDSTEIN, M.E., DURBIN, P.A. & LEIB, S.J. 1987 Roll–up of vorticity in adverse–pressure–gradient boundary layers. *J. Fluid Mech.* **183**, 325-342.

GOLDSTEIN, M.E. & HULTGREN, L.S. 1988 Nonlinear spatial evolution of an externally excited instability wave in a free shear layer. *J. Fluid Mech.* **197**, 295-330.

GOLDSTEIN, M.E. & LEE, S.S. 1992 Fully coupled resonant-triad interaction in an adverse-pressure-gradient boundary layer. *J. Fluid Mech.* **245**, 523-551.

GOLDSTEIN, M.E. & LEIB, S.J. 1989 Nonlinear evolution of oblique waves on compressible shear layers. *J. Fluid Mech.* **207**, 73-96.

HRISTOV, T.S., MILLER, S.D. & FRIEHE, C.A. 2003 Dynamical coupling of wind and ocean waves through wave-induced air flow. *Nature* **442**, 55-58.

JANSSEN, P. 2004 *The Interaction of Ocean Waves and Wind.* Cambridge University Press.

LEE, S.S. 1997 Generalized critical-layer analysis of fully coupled resonant-triad interactions in boundary layers. *J. Fluid Mech.* **347**, 71-103.

LEE, S.S. 2012 Nonlinear interaction of wind-driven oblique surface waves and parametric growth of lower frequency modes. *J. Fluid Mech.* **707**, 150-190.

LEE, S.S. & WUNDROW, D.W. 2011 Transition from long-crested to short-crested seas by wind-wave interaction. *ISOPE, 21st International Offshore (Ocean) & Polar Engineering Conference, June 19-24, 2011, Maui, HI.*

MILES, J.W. 1957 On the generation of surface waves by shear flows. *J. Fluid Mech.* **3**, 185-204.

MILES, J.W. 1993 Surface-wave generation revisited. *J. Fluid Mech.* **256**, 427-441.

MORLAND, L.C. & SAFFMAN, P.G. 1993 Effect of wind profile on the instability of wind blowing over water. *J. Fluid Mech.* **252**, 383-398.

REUTOV, V.P. 1980 The plasma-hydrodynamic analogy and the nonlinear stage of instability of wind waves. *Izv. Atmos. Ocean. Phys.* **16**, 938-943.

WU, X. 1992 The nonlinear evolution of high-frequency resonant-triad waves in an oscillatory Stokes layer at high Reynolds number. *J. Fluid Mech.* **245**, 553-597.

WU, X., LEE, S.S. & COWLEY, S.J. 1993 On the weakly nonlinear three-dimensional instability of shear layers to pairs of oblique waves: the Stokes layer as a paradigm. *J. Fluid Mech.* **253**, 681-721.

WU, X. & STEWART, P.A. 1996 Interaction of phase-locked modes: a new mechanism for the rapid growth of three-dimensional disturbances. *J. Fluid Mech.* **316**, 335-372.

WUNDROW, D.W., HULTGREN, L.S. & GOLDSTEIN, M.E. 1994 Interaction of oblique instability waves with a nonlinear plane wave. *J. Fluid Mech.* **264**, 343-372.

APPENDIX A: RELATIONS BETWEEN J_i AND b_i

For $i = \{p, s, d1, \ldots, dN\}$, $\Phi_i^{(b)}$ can be computed by numerically integrating (44) subject to (46) and (49) below the critical level where $0 \leq z < z_c$. Then the complex constant J_i defined by (48) can also be evaluated as

$$J_i = (1/b_i) \lim_{z \to z_c^-} \Phi_i^{(b)}(z). \tag{A-1}$$

The second shape function $\Phi_i^{(b)}$ becomes purely imaginary on the real axis below the critical level since the boundary conditions (46) and (49) are purely imaginary. Thus, $J_i b_i$ also becomes purely imaginary, or

$$\mathrm{Re}(J_i b_i) = 0. \tag{A-2}$$

By multiplying (44) by $\Phi_i^{(b)*}$, integrating over transverse domain with (52), and substituting (86), we obtain

$$\int_0^\infty \left[|\partial_z \Phi_i^{(b)}|^2 + \left(\gamma_i^2 + \frac{U''}{U - c} \right) |\Phi_i^{(b)}|^2 \right] dz = -J_i^* b_i^* \left(i\pi J_i b_i \frac{U_c''}{U_c'} - \frac{1}{b_i} \right). \tag{A-3}$$

Because the left-hand side of the above equation is real, the term in the parentheses on the right-hand side must be purely imaginary. Therefore,

$$\mathrm{Re}(i\pi J_i b_i U_c''/U_c' - 1/b_i) = 0 \quad \text{and} \quad |J_i| = |U_c' \, \mathrm{Re}(b_i)/(\pi U_c'' b_i^3)|. \tag{A-4}$$

If

$$U''/(U - c) + \gamma_i^2 > 0 \tag{A-5}$$

below the critical level, which is satisfied by the logarithmic wind profile (7), then

$$\partial_z^2 \Phi_i^{(b)}/\Phi_i^{(b)} > 0. \tag{A-6}$$

From above results with (A-1) and (A-6), one can show that (A-2) becomes

$$J_i b_i = -i|J_i b_i|. \tag{A-7}$$

By putting (A-7) into (A-4), we find that

$$J_i = -iU_c' \mathrm{Re}(b_i)/(\pi U_c'' |b_i|^2 b_i). \tag{A-8}$$

This page intentionally left blank.

APPENDIX B: SYSTEM OF CRITICAL-LAYER EQUATIONS

The normalized variables in (79)–(81) and

$$\{A_\imath,\ Q_\imath\} = \{\tilde{A}_\imath/\hat{\kappa},\ \gamma_\imath\tilde{Q}_\imath^{(1)}/\beta_\imath\}(\sqrt{M/U_c'}/\hat{\kappa}^2)\mathrm{e}^{\mathrm{i}\hat{\alpha}_\imath(X_o+\tilde{\zeta}_o\bar{t})} \tag{B-1}$$

are used for the critical-layer equations. The variables represented by $\tilde{Q}_\jmath^{(2)}$ in (78) are also normalized as

$$\left\{U_\jmath^{(2)}, V_\jmath^{(2)}, W_\jmath^{(2)}, P_\jmath^{(2)}\right\} = \left\{\frac{\bar{\alpha}}{\bar{\beta}}\tilde{U}_\jmath^{(2)},\ \tilde{V}_\jmath^{(2)},\ \frac{\mathrm{i}}{\bar{\beta}\hat{\kappa}}\tilde{W}_\jmath^{(2)},\ \frac{\bar{\beta}}{\bar{\alpha}\hat{\kappa}U_c'}\tilde{P}_\jmath^{(2)}\right\}\frac{\bar{\alpha}M}{\bar{\beta}\hat{\kappa}^3}\,\mathrm{e}^{\mathrm{i}\hat{\alpha}_\jmath(X_o+\tilde{\zeta}_o\bar{t})}, \tag{B-2}$$

with $\hat{\alpha}_\jmath$ given below by (B-7).

The system of normalized equations, which we refer to as the critical-layer equations, now becomes at the leading order, for $\imath = \{p, s, d1, \ldots, dN\}$,

$$\mathcal{L}_\imath Q_\imath = \hat{\alpha}_\imath A_\imath, \tag{B-3}$$

subject to the transverse boundary condition, $Q_\imath \sim 1/\zeta$ as $\zeta \to \infty$. We have put

$$\mathcal{L}_\imath \equiv \frac{\partial}{\partial\bar{t}} + \mathrm{i}\hat{\alpha}_\imath\zeta - \lambda\frac{\partial^2}{\partial\zeta^2}. \tag{B-4}$$

The second-order critical-layer equations are written as

$$\mathcal{L}_\jmath\{V_\jmath^{(2)},\ W_{\jmath\zeta\zeta}^{(2)},\ U_{\jmath\zeta}^{(2)}\} = \{R_{v\jmath}^{(2)},\ R_{w\jmath}^{(2)},\ R_{u\jmath}^{(2)}\}, \tag{B-5}$$

$$W_{\jmath\zeta}^{(2)} = \hat{\alpha}_\jmath U_\jmath^{(2)} + \hat{\beta}_\jmath V_\jmath^{(2)}, \quad P_{\jmath\zeta}^{(2)} = 0, \tag{B-6}$$

for $\jmath = \{p,\ 0,\ 2p,\ s,\ p+s,\ d1,\ \ldots,\ d(N{+}1)\}$, with

$$\hat{\alpha}_0 = 0, \quad \hat{\alpha}_{2p} = 2\hat{\alpha}_p, \quad \hat{\alpha}_{p+s} = \hat{\alpha}_p + \hat{\alpha}_s, \quad \hat{\alpha}_{dn} = n\hat{\alpha}_p - \hat{\alpha}_s, \tag{B-7}$$

$$\hat{\beta}_0 = 0, \quad \hat{\beta}_{2p} = 2\hat{\beta}_p, \quad \hat{\beta}_{p+s} = \hat{\beta}_p + \hat{\beta}_s, \quad \hat{\beta}_{dn} = n\hat{\beta}_p - \hat{\beta}_s. \tag{B-8}$$

For the primary, secondary and difference modes (B-5) and (B-6) become

$$\mathcal{L}_p V_p^{(2)} = -\mathrm{i}\hat{\beta}_p P_p^{(2)} - \tfrac{1}{2}(\bar{\alpha}/\bar{\beta})\sqrt{M/U_c'}\,U_c''\,\hat{\alpha}_p\hat{\mu}_p(\zeta + \tilde{\zeta}_o)^2 Q_p, \tag{B-9}$$

$$\mathcal{L}_p W_{p\zeta\zeta}^{(2)} = \mathrm{i}(\bar{\alpha}/\bar{\beta})\sqrt{M/U_c'}\,U_c''\,\hat{\alpha}_p\hat{\gamma}_p A_p, \tag{B-10}$$

$$W_{p\zeta}^{(2)} = \hat{\alpha}_p U_p^{(2)} + \hat{\beta}_p V_p^{(2)}, \quad P_{p\zeta}^{(2)} = 0, \tag{B-11}$$

$$\begin{aligned}
\mathcal{L}_s V_s^{(2)} = {}&-\mathrm{i}\hat{\beta}_s P_s^{(2)} - \tfrac{1}{2}(\bar{\alpha}/\bar{\beta})\sqrt{M/U_c'}\,U_c''\,\hat{\alpha}_s\hat{\mu}_s(\zeta + \tilde{\zeta}_o)^2 Q_s \\
&- \hat{\gamma}_p\hat{\mu}_{d1} A_p Q_{d1\,\zeta}^* - \hat{\gamma}_{d1}\hat{\mu}_p A_{d1}^* Q_{p\,\zeta} - \mathrm{i}\bar{\nu}_{p-d}^{(1)}\hat{\alpha}_{d2}\hat{\mu}_p\hat{\mu}_{d1}Q_p Q_{d1}^*,
\end{aligned} \tag{B-12}$$

$$\begin{aligned}
\mathcal{L}_s W_{s\zeta\zeta}^{(2)} = {}&\mathrm{i}(\bar{\alpha}/\bar{\beta})\sqrt{M/U_c'}\,U_c''\,\hat{\alpha}_s\hat{\gamma}_s A_s - \bar{\nu}_{p-d}^{(1)}\Big[\hat{\alpha}_p\hat{\gamma}_p\hat{\mu}_{d1}A_p Q_{d1\,\zeta\zeta}^* \\
&+ \hat{\alpha}_{d1}\hat{\gamma}_{d1}\hat{\mu}_p A_{d1}^* Q_{p\,\zeta\zeta} + \mathrm{i}2\bar{\nu}_{p-d}^{(1)}\hat{\alpha}_p\hat{\alpha}_{d1}\hat{\mu}_p\hat{\mu}_{d1}(Q_p Q_{d1}^*)_\zeta\Big],
\end{aligned} \tag{B-13}$$

$$W_{s\,\zeta}^{(2)} = \hat{\alpha}_s U_s^{(2)} + \hat{\beta}_s V_s^{(2)}, \qquad P_{s\,\zeta}^{(2)} = 0, \tag{B-14}$$

$$\mathcal{L}_{dn} V_{dn}^{(2)} = -\mathrm{i}\hat{\beta}_{dn} P_{dn}^{(2)} - \tfrac{1}{2}(\bar{\alpha}/\bar{\beta})\sqrt{M/U_c'}\, U_c'' \,\hat{\alpha}_{dn}\hat{\mu}_{dn}(\zeta + \tilde{\zeta}_o)^2 Q_{dn} - \hat{\gamma}_p \hat{\mu}_{d(n+1)} A_p^* Q_{d(n+1)\,\zeta}$$

$$-\hat{\gamma}_{d(n+1)}\hat{\mu}_p A_{d(n+1)} Q_{p\,\zeta}^* + \mathrm{i}\bar{\nu}_{p-d}^{(n+1)} \hat{\alpha}_{d(n+2)}\hat{\mu}_p \hat{\mu}_{d(n+1)} Q_p^* Q_{d(n+1)} + \hat{\gamma}_p \hat{\mu}_{d(n-1)} A_p Q_{d(n-1)\,\zeta}$$

$$+\hat{\gamma}_{d(n-1)}\hat{\mu}_p A_{d(n-1)} Q_{p\,\zeta} - \mathrm{i}\bar{\nu}_{p-d}^{(n-1)} \hat{\alpha}_{d(n-2)}\hat{\mu}_p \hat{\mu}_{d(n-1)} Q_p Q_{d(n-1)}, \tag{B-15}$$

$$\mathcal{L}_{dn} W_{dn\,\zeta\zeta}^{(2)} = \mathrm{i}(\bar{\alpha}/\bar{\beta})\sqrt{M/U_c'}\, U_c'' \,\hat{\alpha}_{dn}\hat{\gamma}_{dn} A_{dn} + \bar{\nu}_{p-d}^{(n+1)} \left[\hat{\alpha}_p \hat{\gamma}_p \hat{\mu}_{d(n+1)} A_p^* Q_{d(n+1)\,\zeta\zeta} \right.$$

$$+\hat{\alpha}_{d(n+1)}\hat{\gamma}_{d(n+1)}\hat{\mu}_p A_{d(n+1)} Q_{p\,\zeta\zeta}^* - \mathrm{i}2\bar{\nu}_{p-d}^{(n+1)}\hat{\alpha}_p \hat{\alpha}_{d(n+1)}\hat{\mu}_p \hat{\mu}_{d(n+1)} (Q_p^* Q_{d(n+1)})_\zeta \Big]$$

$$+\bar{\nu}_{p-d}^{(n-1)} \left[\hat{\alpha}_p \hat{\gamma}_p \hat{\mu}_{d(n-1)} A_p Q_{d(n-1)\,\zeta\zeta} - \hat{\alpha}_{d(n-1)}\hat{\gamma}_{d(n-1)}\hat{\mu}_p A_{d(n-1)} Q_{p\,\zeta\zeta} \right.$$

$$-\mathrm{i}2\bar{\nu}_{p-d}^{(n-1)}\hat{\alpha}_p \hat{\alpha}_{d(n-1)}\hat{\mu}_p \hat{\mu}_{d(n-1)} (Q_p Q_{d(n-1)})_\zeta \Big], \tag{B-16}$$

$$W_{dn\,\zeta}^{(2)} = \hat{\alpha}_{dn} U_{dn}^{(2)} + \hat{\beta}_{dn} V_{dn}^{(2)}, \qquad P_{dn\,\zeta}^{(2)} = 0, \tag{B-17}$$

where

$$\hat{\mu}_\imath = \hat{\beta}_\imath/\hat{\gamma}_\imath = \sin\theta_\imath \quad \text{for} \quad \imath = \{p, s\}, \qquad \hat{\mu}_{dn} = \hat{\beta}_{dn}/\hat{\gamma}_{dn} \quad \text{for} \quad n = 1, 2, \ldots, N+1, \tag{B-18}$$

$$\bar{\nu}_{p-d}^{(n)} \equiv \hat{\beta}_p/\hat{\alpha}_p - \hat{\beta}_{dn}/\hat{\alpha}_{dn}. \tag{B-19}$$

APPENDIX C: NORMALIZATION PARAMETERS $\bar{\alpha}$, $\bar{\beta}$, $\hat{\kappa}$, M AND $\tilde{\zeta}_O$

The normalization parameters are chosen as

$$\bar{\alpha} = \alpha_{30}, \quad \bar{\beta} = \beta_{30}, \quad \theta_{30} = \pi/6, \tag{C-1}$$

$$\hat{\kappa} = -\pi c U_c'' |b_{30}|^2 (\cos \theta_{30}) / [2\bar{\alpha} U_c'^2 \tanh(\gamma_{30} H)], \tag{C-2}$$

$$\tilde{\zeta}_o = -U_c' R_{30}/(\pi U_c'' \hat{\alpha}_{30} |b_{30}|^2), \quad \sqrt{M} = \bar{\beta}^2 |J_{30}||b_{30}|^2 (\cos \theta_{30})/(\bar{\alpha}^2 \sqrt{U_c'}), \tag{C-3}$$

where the subscript 30 denotes the quantities of a surface wave with propagation angle of 30 degrees. The choice of $\theta_{30} = \pi/6$ is arbitrary. According to Fjørtoft's theorem, it is assumed that $U_c'' < 0$ and $U_c' > 0$, so that $\hat{\kappa}$ and $\sqrt{M}$ are positive. From (79) and (C-1), one can show that

$$\hat{\alpha}_{30} = \hat{\beta}_{30} = 1. \tag{C-4}$$

This page intentionally left blank.

APPENDIX D: CRITICAL-LAYER JUMPS FOR THE DIFFERENCE MODES

If the solution (89) is substituted for A_p, the variables $\Lambda_n^\pm(\bar{t})$, $F_n^\pm(\bar{t})$ and $G_n^\pm(\bar{t})$ in (83) become

$$\Lambda_n^\pm = \pm i\pi(\bar{\alpha}/\bar{\beta})\sqrt{M/U_c'}\, U_c''(\hat{\gamma}_{dn}/\hat{\alpha}_{dn})\, A_{dn}(\bar{t}), \tag{D-1}$$

$$F_n^\pm = \mp \bar{a}_p^\mp C_{c\pm}^{(n)} e^{\bar{\kappa}_p^\mp \bar{t}} \left[\nu_n \hat{\gamma}_{d(n\pm1)} \int_0^\infty E_{a\pm}^{(n)}(\tau)\, E_{c\pm}^{(n)}(\tau)\, \tau^2\, A_{d(n\pm1)}(\bar{t}-\tau)\, d\tau \right.$$
$$\left. - C_{d\pm}^{(n)} \int_0^\infty \int_0^\infty E_{u\pm}^{(n)}(\tau_1,\tau_2)\, E_{c\pm}^{(n)}(\tau_1+\tau_2)\, \tau_1\, A_{d(n\pm1)}(\bar{t}-\tau_1-\tau_2)\, d\tau_1 d\tau_2 \right], \tag{D-2}$$

$$G_n^\pm = \mp \bar{a}_p^\mp C_{a\pm}^{(n)} e^{\bar{\kappa}_p^\mp \bar{t}} \left[\nu_n \hat{\gamma}_p \int_0^\infty E_{b\pm}^{(n)}(\tau)\, E_{c\pm}^{(n)}(\tau)\, \tau^2\, A_{d(n\pm1)}(\bar{t}-\tau)\, d\tau \right.$$
$$\left. - C_{b\pm}^{(n)} \int_0^\infty \int_0^\infty E_{v\pm}^{(n)}(\tau_1,\tau_2)\, E_{c\pm}^{(n)}(\tau_1+\tau_2)\, \tau_1\, A_{d(n\pm1)}(\bar{t}-\tau_1-\tau_2)\, d\tau_1 d\tau_2 \right], \tag{D-3}$$

where

$$\nu_n \equiv n - \hat{\nu}, \qquad \hat{\nu} \equiv \hat{\alpha}_s/\hat{\alpha}_p, \tag{D-4}$$

$$C_{a\pm}^{(n)} = 2\pi(1 \pm \nu_n)^3 \hat{\alpha}_p^2 \bar{\nu}_{p-d}^{(n\pm1)} \hat{\mu}_{d(n\pm1)}, \qquad C_{b\pm}^{(n)} = 2\hat{\alpha}_{d(n\pm1)} \bar{\nu}_{p-d}^{(n\pm1)} \hat{\mu}_p,$$
$$C_{c\pm}^{(n)} = \pi\hat{\alpha}_p C_{b\pm}^{(n)}, \qquad C_{d\pm}^{(n)} = C_{a\pm}^{(n)}/[\pi\hat{\alpha}_p(1\pm\nu_n)^2], \tag{D-5}$$

$$E_{a\pm}^{(n)}(\tau) = \exp\left[-\tfrac{1}{3}\lambda\hat{\alpha}_p^2\nu_n^2(1\pm\nu_n)\tau^3\right], \qquad E_{b\pm}^{(n)}(\tau) = \exp\left[-\tfrac{1}{3}\lambda\hat{\alpha}_p^2\nu_n^2(1\pm\nu_n)^2\tau^3\right],$$
$$E_{c\pm}^{(n)}(\tau) = \exp\left[-(1\pm\nu_n)\bar{\kappa}_p^\mp\tau\right], \tag{D-6}$$

$$E_{u\pm}^{(n)}(\tau_1,\tau_2) = \exp\left[-\tfrac{1}{3}\lambda\hat{\alpha}_p^2\left\{\nu_n^2\tau_1^3 + (1\pm\nu_n)^2\tau_2^3 + \{\pm\nu_n\tau_1 + (1\pm\nu_n)\tau_2\}^3\right\}\right], \tag{D-7}$$

$$E_{v\pm}^{(n)}(\tau_1,\tau_2) = \exp\left[-\tfrac{1}{3}\lambda\hat{\alpha}_p^2(1\pm\nu_n)^2\left\{(1\pm\nu_n)(\nu_n^2\tau_1^3 + \tau_2^3) + (\mp\nu_n\tau_1+\tau_2)^3\right\}\right], \tag{D-8}$$

with $\bar{a}_p^+ = a_p$, $\bar{a}_p^- = a_p^*$, $\bar{\kappa}_p^+ = \kappa_p$, $\bar{\kappa}_p^- = \kappa_p^*$, $A_{d0} = -A_s^*$ and $\hat{\mu}_p$, $\hat{\mu}_{dn}$, $\bar{\nu}_{p-d}^{(n)}$ in (B-18) and (B-19).

This page intentionally left blank.

APPENDIX E: VARIABLES g_{n-1}, h_n, s_{asy} AND r_{asy}

When λ is $O(1)$, g_{n-1} and h_n in (124) and (125) become

$$g_{n-1} = -\frac{16(\mathrm{Re}\kappa_p)^6(n-1+\xi)^3(n-1+\xi+\nu_N)^3\,[I_1(n)+I_2(n)]\,[I_3^*(n-1)+I_4^*(n-1)]}{C_{a-}^{(N)}C_{a+}^{(N-1)}\left(\nu_N\hat{\gamma}_p - C_{b-}^{(N)}/2\right)\left(\nu_{N-1}\hat{\gamma}_p - C_{b+}^{(N-1)}/2\right)}, \tag{E-1}$$

$$h_n = 4(\mathrm{Re}\kappa_p)^3(n+\xi)^3\,[I_3(n)+I_4(n)]\,/\left[C_{a-}^{(N)}(\nu_N\hat{\gamma}_p - C_{b-}^{(N)}/2)\right], \tag{E-2}$$

where

$$I_1(n) = -C_{a+}^{(N-1)}\nu_{N-1}\hat{\gamma}_p \int_0^\infty E_{b+}^{(N-1)}(\tilde{\tau}_1)\,\mathrm{e}^{-[2(n+N-1)\mathrm{Re}\kappa_p-\hat{\nu}\hat{\kappa}_p^*+\hat{\kappa}_s^*]\tilde{\tau}_1}\,\tilde{\tau}_1^2\,d\tilde{\tau}_1, \tag{E-3}$$

$$I_2(n) = C_{a+}^{(N-1)}C_{b+}^{(N-1)} \int_0^\infty\int_0^\infty E_{v+}^{(N-1)}(\tilde{\tau}_1,\tilde{\tau}_2)\,\mathrm{e}^{-[2(n+N-1)\mathrm{Re}\kappa_p-\hat{\nu}\hat{\kappa}_p^*+\hat{\kappa}_s^*](\tilde{\tau}_1+\tilde{\tau}_2)}\,\tilde{\tau}_1\,d\tilde{\tau}_2 d\tilde{\tau}_1, \tag{E-4}$$

$$I_3(n) = C_{a-}^{(N)}\nu_N\hat{\gamma}_p \int_0^\infty E_{b-}^{(N)}(\tilde{\tau}_1)\,\mathrm{e}^{-(2n\mathrm{Re}\kappa_p+\hat{\nu}\hat{\kappa}_p+\hat{\kappa}_s^*)\tilde{\tau}_1}\,\tilde{\tau}_1^2\,d\tilde{\tau}_1, \tag{E-5}$$

$$I_4(n) = -C_{a-}^{(N)}C_{b-}^{(N)} \int_0^\infty\int_0^\infty E_{v-}^{(N)}(\tilde{\tau}_1,\tilde{\tau}_2)\,\mathrm{e}^{-(2n\mathrm{Re}\kappa_p+\hat{\nu}\hat{\kappa}_p+\hat{\kappa}_s^*)(\tilde{\tau}_1+\tilde{\tau}_2)}\,\tilde{\tau}_1\,d\tilde{\tau}_2 d\tilde{\tau}_1, \tag{E-6}$$

and ξ, $\hat{\nu}$, ν_n, $C_{a\pm}^{(n)}$, $C_{b\pm}^{(n)}$, $E_{b\pm}^{(n)}$ and $E_{v\pm}^{(n)}$ are given by (126), (D-4)–(D-6) and (D-8).

The coefficients s_{asy} and r_{asy} in (129) and (130) are

$$s_{asy} = \left[s_0/(8\sqrt{3}\,\pi^{5/2})\right]\Gamma^3(\xi)\Gamma^3(\xi+\nu_N)\left\{(\nu_N/\mathrm{Re}\kappa_p)^3\hat{\varphi}_a^{(inv)}/4\right\}^{-\xi-\nu_N/2+7/12}\prod_{m=1}^\infty g_{m-1}, \tag{E-7}$$

$$r_{asy} = (1/2)(\nu_N\mathrm{Re}\kappa_p)^{-3/2}\,\hat{\varphi}_b^{(inv)}\left(\hat{\varphi}_a^{(inv)}\right)^{-1/2}. \tag{E-8}$$

This page intentionally left blank.

Distribution

	Hard Copies	Digital Copies			Hard Copies	Digital Copies
Defense Technical Information Center 8725 John J. Kingman Road Ft. Belvoir, VA 22060-6218		1	**NSWC, CARDEROCK DIVISION INTERNAL DISTRIBUTION**			
			Code	Name		
			809	D. Intolubbe	1	1
			83	Technical Data Library	1	1
			1033	TIC - SCRIBE		1
			012	J. Price		1
			801	J. Gorski		1
			85	J. Brown		1
			854	M. Donnelly		1
			851	T. Smith		1
			854	R. Hurwitz	1	1
			851	S. S. Lee	1	1

WARFARE CENTERS
Carderock